NASA CONTRACTOR REPORT

NASA CR-266

THE BUCKLING STRENGTH OF FILAMENT-WOUND CYLINDERS UNDER AXIAL COMPRESSION

by J. Tasi, A. Feldman, and D. A. Stang

NASA CR-266

THE BUCKLING STRENGTH OF FILAMENT-WOUND

CYLINDERS UNDER AXIAL COMPRESSION
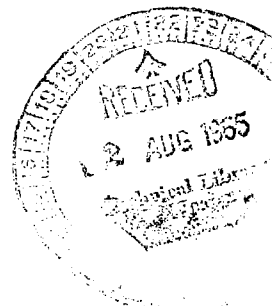
By J. Tasi, A. Feldman, and D. A. Stang

CONTENTS

ACKNOWLEDGEMENT

SUMMARY

The buckling strengths of eleven axially compressed filament-wound cylinders with diameter to thickness ratios ranging from 167 to 643 are determined experimentally and analytically. The analytical predictions of buckling loads are made by using linear anisotropic shell theory. The results of the compression tests generally indicate that the cylinders buckled at 65 to 85% of the loads predicted by linear analysis. The composite moduli for each of the cylinders are determined experimentally and are in reasonable agreement with the theory of S. Tsai.

SYMBOLS

$[A]$	In-plane stiffness matrix
a_{ij}	Element of characteristic determinant
A_k, B_k, C_k	Modal amplitudes
$[B]$	Coupling stiffness matrix
c	Cos φ, also used as a superscript or subscript to indicate circumferential layer
C	S. Tsai's contiguity factor
$[C]$	Modulus matrix
$C_{11}{}^{c}$	Composite modulus perpendicular to the fibers
$C_{12}{}^{c}$	Composite modulus representing Poisson's ratio effect
$C_{22}{}^{c}$	Composite modulus in the fiber direction
$C_{66}{}^{c}$	Composite shear modulus
D	Mean cylinder diameter
$[D]$	Bending stiffness matrix
$e_{xx}, e_{\theta\theta}, e_{x\theta}$	Strains
E_f	Young's modulus of filament
E_m	Young's modulus of matrix
$E_{11}{}^{c}$	Composite Young's modulus perpendicular to the fibers $= C_{11}{}^{c} \left(1 - \nu_{12} \cdot \nu_{21}\right)$

$E_{22}{}^c$ Composite Young's modulus in the fiber direction

$$= C_{22}{}^c \left(1 - \nu_{12} \cdot \nu_{21}\right)$$

h   Total thickness of shell

h_c Thickness of a circumferential layer

h_p Total thickness of a polar layer

i   Indicates initial stress state; also used to indicate $(-1)^{\frac{1}{2}}$

j   Indicates polar half-layer; also used to indicate number of iterations

k   Filament misalignment factor

κ_{xx}, $\kappa_{\theta\theta}$, $\kappa_{x\theta}$ Curvatures

L   Cylinder length

m   Number of axial half-waves

[M]   Symmetric matrix relating modulus to in-plane stiffness

M_{xx}, $M_{\theta\theta}$, $M_{x\theta}$, $M_{\theta x}$ Unit bending moments

n   Number of circumferential waves

N_{xx}, $N_{\theta\theta}$, $N_{x\theta}$, $N_{\theta x}$ Unit stress resultants

p   Pressure, also used as a superscript or subscript to indicate polar layer

R   Mean cylinder radius

s   sin φ

u, v, w	Axial, circumferential, and radial displacements
x, θ, z	Axial, angular, and radial coordinates
x', y', z'	Cartesian coordinate system
$\epsilon_{\theta\theta}{}^{o}$, $\epsilon_{xx}{}^{o}$, $\epsilon_{x\theta}{}^{o}$	In-plane strains
γ_f	Specific gravity of filament
γ_m	Specific gravity of matrix
λ	Axial wave number
ν_f	Poisson's ratio of filament
ν_m	Poisson's ratio of matrix
ν_{12}	Major Poisson's ratio of composite
ν_{21}	Minor Poisson's ratio of composite
φ	Angle of polar winding
σ_{xx}, $\sigma_{\theta\theta}$, $\sigma_{x\theta}$	Stresses

I. INTRODUCTION

Experimental data on buckling of filament-wound cylinders under axial compression have been obtained by Young,[1] Card and Peterson,[2] and Sargent (see Ravenhall[3]). The cylinders tested had diameter to thickness ratios ranging from 25 to 304. In general, a reasonable comparison was achieved between the buckling loads predicted by small deflection orthotropic shell theory and the test data. In addition, Card and Peterson noted the coupling between shear failure and buckling when resin stresses are high enough at the buckling load to cause plastic flow in the resin.

This report describes an experimental and analytical study of the buckling strength of eleven filament-wound cylinders under axial compression. The cylinders fabricated for this study have diameter to thickness ratios of 167 to 643 and consist of three composite layers. Fabrication procedures for the cylinders are given in Appendix A. One layer is a polar wrap consisting of two half-layers at angles of $+\varphi$ and $-\varphi$ with respect to the longitudinal axis of the cylinder ($0 \leq \varphi < 9$ deg). The polar wrap is enclosed by an inner and an outer circumferential wrap. The three layers have the same nominal thickness. This combination is chosen because it is efficient for internal pressure and minimizes the effects of initial imperfections on buckling strength by providing circumferential in-plane and bending stiffening.[4, 5, and 6] All of the cylinders studied have in-plane and bending stiffness matrices of orthotropic form. Also, the cylinders whose middle layers are not oriented axially produce an anisotropic coupling between stretching and shear of the form described by Reissner and Stavsky.[7]

Analytical predictions for buckling loads were obtained by using linear anisotropic shell theory. The results of the compression tests indicate that the cylinders buckled at 65 to 85% of the loads predicted by classical linear analysis. The buckling mode was coupled with catastrophic shear failure in the smaller cylinders. The larger cylinders buckled into the classical diamond-shaped pattern with the basic integrity of the cylinder maintained.

The composite moduli required for the buckling analysis are determined for each cylinder from experimental test data. The data are obtained by the classical method of using three tests: torsion, internal pressure, and axial tension or compression. It is demonstrated analytically that the anisotropic coupling between stretching and shear only influences the determination of the moduli by terms of the order of the square of the ratio of the thickness of the cylinder to the radius of the cylinder. Thus, because of the thinness of the cylinders, the anisotropic coupling has a negligible effect on the experimental determination of moduli. Also, the moduli obtained from the experimental data are compared with those predicted by the theory of S. Tsai.[8] In general, agreement is good when a value of 0.3 is assigned to his continguity factor.

II. ANALYTICAL PROCEDURE

The buckling loads for clamped filament-wound cylinders under uniform axial compression are analytically determined by using linear anisotropic shell theory. The general procedure for obtaining buckling solutions for anisotropic cylinders with specified boundary conditions has been given by Cheng and Ho.[9] For the sake of completeness, the derivation of the solution is given in Appendix B and is briefly outlined here.

The displacement equations of equilibrium that are used are obtained by combining Flügge's[10] stress equations of equilibrium and strain-displacement expressions with an anisotropic stress-strain relationship. The eighth order system of displacement equations governing the stability of the cylinder are solved by first assuming a wave form for the displacement field in terms of the axial and angular coordinates.[9 and 11] The requirement that the equations of equilibrium be satisfied yields a characteristic equation governing the eight axial wave numbers that are permitted for a given load. Since each axial wave number satisfies the characteristic equation, the displacement modes corresponding to each wave number can be superimposed. The modal amplitudes are governed by the requirement that the prescribed end conditions be satisfied. The lowest axial load that simultaneously satisfies the differential equations of equilibrium and the end conditions is the critical buckling load.

The numerical solution for the buckling load is obtained in the following manner. First, a lower bound for the load is obtained from the characteristic equation by accepting whatever boundary conditions occur with an integral number of half-waves specified in the axial direction.* For a clamped cylinder ($w = v = u = \partial w/\partial x = 0$ at $x = \pm L/2$), the buckling load is raised. With a given number of circumferential waves and with specified geometric and material properties of the clamped cylinder, the

---

*For the particular case of an orthotropic cylinder, the end conditions for the lower bound solution are the usual mixed or "simple" supports on a right-circular section, that is, $w = v = N_{xx} = M_{xx} = 0$ at $x = \pm L/2$. With a general anisotropic medium, the end conditions corresponding to the lower bound solution depend on the degree of anisotropy.

buckling load is found by an interval halving procedure. The lower bound solution is used for the first estimate. The initial increment is also obtained from the solutions of the characteristic equation by choosing an increment that is less in magnitude than the difference between the buckling load for the fundamental mode and the next higher mode. With each trial buckling load, an eighth order polynomial equation, obtained by expanding the characteristic determinant, is solved for the eight axial wave numbers by using Muller's method.[12] After the wave numbers are computed, the boundary determinant obtained by requiring clamped conditions is evaluated by Crout reduction. The iteration is continued until the sign of the boundary determinant changes. The interval is then halved, and the process is repeated until sufficient accuracy is achieved. Buckling loads corresponding to different numbers of circumferential waves can be found, if necessary, to determine the minimum buckling load.

The stiffnesses required for the buckling analysis are obtained from three simple experiments. The tests used are internal pressure, axial tension or axial compression, and torsion, with principal strains measured throughout. The load-strain slopes from the three tests provide a direct determination of the in-plane stiffness matrix. By definition, the in-plane stiffness matrix is the integral of the composite moduli over the thickness of the shell. The integration yields four simultaneous, symmetric, algebraic, nonhomogeneous equations relating the principal composite orthotropic moduli for filament-wound construction to the in-plane stiffnesses. The equations are simply inverted by Crout reduction. The moduli thus determined are used to compute the bending stiffness and the coupling stiffness matrices used in the buckling analysis. The derivation of the equations required to compute the stiffnesses and moduli from the test data is given in Appendix C.

III. EXPERIMENTAL PROCEDURE

The general procedure used for determining stiffnesses and the buckling strength of each cylinder was as follows. End plates were shrink fitted to the cylinder and external ring clamping was applied. The ten to twelve strain gages on the cylinder were used to first record strains up to 500 microinches/in. in each of the three tests used to determine initial stiffnesses, and then were used to record strains during the buckling test. The locations and orientations of the strain gages are given in Fig. 1. The internal pressure test was conducted first. This test provided a good check on strain gage performance as well as serving its intended purpose for determining stiffness. Torsion arms were then fitted to the end plates, and a pure torque was applied to the cylinder in a torsion frame. The torque arms were then removed and the cylinder was placed in a universal testing machine for the axial tension test. Afterward, because of the possibility of slippage during the tension test, the end clamping rings were loosened to permit reseating the end plates against the ends of the cylinder. The end plates were then reclamped and the cylinder tested in axial compression until buckling occurred.

After the buckling test, four photomicrographs were taken of the cross section of the cylinder at widely spaced locations. The photomicrographs provided layer thicknesses and an estimate of winding quality. If buckling occurred in a confined region, the photomicrographs were taken only in that region. The geometric parameters of each cylinder are listed in Table 1.

Before each test, all strain gage channels were zeroed with a switching and balancing unit. After each increment of load, the gages were run through quickly to prevent gage heating and subsequent zero drift. This technique was followed because the filament-wound composite has a low coefficient of thermal conductivity. The technique was found to be generally successful in preventing zero drift. Raw data were plotted in the form of pressure, torque, or force versus strain for each strain gage read. The slopes were then picked from the graphs.

IV. RESULTS

A. EXPERIMENTAL RESULTS

A summary of the averaged load-strain slopes used to determine stiffnesses and moduli for each cylinder is given in Table 2. An indication of the individual results for each strain gage, throughout the complete sequence of testing, is given for Cylinder 9 (D = 24 in.) in Fig. 2 thru 5. The nature of the buckling failures in the 6, 12, 18, and 24-in. dia* cylinders is indicated in Fig. 6 thru 12.

The behavior of the specimens with internal pressure loading was as expected. All strain gages indicated extensional deformation with the largest output from the circumferential gages. A netting analysis would predict equal strains for the longitudinal and circumferential directions. The isotropic influence of the resin, however, produced a composite result between a balanced design (equal strain) and an isotropic material (1:2 ratio for strain). The strain gages generally indicated a linear behavior with negligible hysteresis. Hysteresis was quite noticeable, however, in Cylinders 8 and 9 (Fig. 2). This may have been due to not letting the pressure gage stabilize sufficiently during unloading for the tanks with large volume, or it may have been due to strain gage drift.

In general, the data from the tension stiffness tests indicate a remarkably linear behavior with little hysteresis. In this respect, the tension data of Gages 4 and 5 of Cylinder 9 (Fig. 3) are not typical of the gages on the other cylinders. The results of the torsion tests also indicate little hysteresis or non-linearity. The results of the torsion test on Cylinder 9 are shown in Fig. 4, with the principal compression and tension strains plotted in the same direction to facilitate a comparison of the slopes. It should be noted that some of the cylinders were loaded to full test pressure, tension and/or torsion before the actual stiffness test was conducted. Some cylinders were not preloaded. However, preloading appeared to have no effect on the quality of the results, in either linearity or hysteresis.

---

*Diameter.

With the larger diameter cylinders, there was some difficulty in applying the tension loads required to achieve 500 microinches/in. in the axial strain gages because of slippage of the end plates. The clamping force was then considerably increased by additional tightening of the clamping screws so that no slippage occurred. Unfortunately, keeping the same degree of clamping during the compression test appeared to affect the buckling load and the character of the buckles. This is explained in more detail later.

The axial compression loads that buckled the cylinders are listed in Table 2. For all the cylinders except 6, 7, and 8, the values are as expected. The failures were sudden and without warning; loads dropped off precipitously. All four 6-in. diameter cylinders experienced a catastrophic shear failure coupled with diamond-shaped buckles. The plastic behavior of the composite was most noticeable in Cylinder 1, which failed at 14,020 lb while the load was being maintained for the recording of dial and strain gage readings.* The 6-in. dia cylinders with nominal L/D = 5 had buckles only near an end clamping plate (Fig. 6). Figure 7 shows a view of the inside of the same cylinder after the end plates were removed. The 6-in. dia cylinders with nominal L/D = 1 had buckles that covered one-third to one-half the length of the cylinders. Figure 8 is a view of Cylinder 1, unloaded, with the buckle diamonds outlined with a china-marking pencil.

In the larger cylinders, the diamond-shaped buckles occurred with little visual evidence of permanent damage. Figure 9 is a view of Cylinder 4, just after buckling, showing general absence of wall rupture.† In no case did the diamond buckles occur completely around the cylinder. Generally, they only encompassed about three-quarters of the circumference. This is due, of course, to slight variations in the wall construction that trigger the buckle and to the use of a swivel loading head. Once buckling starts, the loading head twists and tends to relieve the unbuckled portions. Within groups of cylinders of the same size, buckling

---

*Strain gage readings were taken after every 1000-lb increment of compression load because of the usefulness of the gages in determining compression moduli. After the experience with Cylinder 1, however, this practice was followed only up to 9000 to 13,000 lb, and then the test was run continuously to failure with only one gage monitored.

†The shear effects were absent because the stresses at buckling were halved by doubling the diameter.

always occurred at the same end (except for Cylinder 7, which was influenced by the end clamping). At first this was thought to be a function of the orientation of the specimens in the testing machine, since the failures occurred at the end loaded by the swivel head. But changes in orientation resulted in continued failure at the same end with respect to the original location on the winding mandrel. Thus, it was concluded that the location of failure was a function of the winding technique and orientation.

The 18-in. dia cylinders exhibited a substantially lower buckling strength and a mode shape that occurred in a narrow region around one clamping plate (Fig. 10). Buckling was not sudden and occurred almost inaudibly. The second 18-in. dia cylinder was instrumented with two strain gages near a clamped end; the gages turned out to be in a region that did not experience the local end buckling. The two gages not only indicated a considerably different slope than the other axial gages, they also recorded a permanent strain. The loading of the 18-in. dia cylinders was discontinued after the first local buckles occurred. The damaged ends were cut off and the rest of the two cylinders were saved for further testing (the testing of the shortened cylinders is described later).

The first 24-in. dia cylinder (Cylinder 8) experienced the same local end buckling result. The load was then continuously increased, however, to find out what would happen. The initial end buckles grew continuously larger until an audible snap occurred and the load dropped. Table 2 shows the two values of buckling load for Cylinder 8 when buckling was first noticed, and when the configuration suddenly changed and the load dropped off. In Fig. 11 the growth of the buckle diamonds is shown by the letters in china-marking pencil. The first buckle occurred at "A." The state corresponding to the higher load in Table 2 is labeled "E." Upon unloading, the buckles disappeared gradually, rather than snapping out.

The local end buckling phenomenon was first suspected to be caused by a lower stiffness near the ends (photomicrographs taken afterward in the buckled region, however, gave no support to this suspicion). Then, an inspection of the photographs of the end buckles showed they occurred directly above the clamping screws (Fig. 10). The consistency of this one-to-one correspondence indicated that the extreme degree of clamping warped the cylinder out of its initial shape and created an initially imperfect geometry that seriously influenced the specimen's buckling resistance. The split clamping rings for the large diameter cylinders were apparently too flexible to distribute the clamping pressure uniformly.

The clamping procedure was corrected before the second 24-in.
dia cylinder (No. 9) was tested. The number of clamping screws
was doubled to 24 and the screws were not made as tight. The
cylinder reached its proper buckling load. No local end buckles
occurred. The failure was sudden and the cylinder buckled into
the classical diamond pattern (Fig. 12). The buckles also dis-
appeared suddenly during unloading. Some of the extreme corners
of the diamond buckles exhibited layer separation. A photomicro-
graph taken of the cylinder cross section is shown in Fig. 13.
In addition to providing layer thickness data and a qualitative
description of the caliber of construction, the photomicrograph
also indicated a crack that was not visually observed after the
test. Figure 14 provides a detailed magnification of the crack.

The last series of tests were on the two 18-in. dia cylinders
whose damaged ends were cut off. The new nominal L/D ratio was
0.76. The cylinder with $\varphi = 0$ was somewhat damaged during the
cutting process. Despite this, the cylinders were subjected to
the complete sequence of testing, and the three stiffness tests
indicated little change in stiffness. The clamping procedure
applied to the shortened 18-in. dia cylinders was similar to that
on Cylinder 9. The number of clamping screws was doubled to 24
and the screws were not made as tight. The buckling strengths
of the two 18-in. dia cylinders were found to be 51 and 89%
greater than the strengths of the same cylinders using the previous
clamping procedure.* No end buckles occurred during the axial
compression tests. The failures were sudden and the cylinders
buckled into the classical diamond pattern (Fig. 15).

B. ANALYTICAL RESULTS

The analysis of the data obtained in this study is summarized
in Tables 3 thru 6.

---

*With a cylinder whose length is of the order of magnitude of
the diameter, small changes in length have negligible influence
on buckling load.

The moduli obtained from the experimental data are given in Table 3. First, the in-plane shear stiffness A_{66} was obtained from an average of the principal tensile and principal compressive small strain data in the torsion test. Next, the in-plane stiffnesses A_{22}, A_{11}, and A_{12} were calculated by combining the small tensile strain data from the internal pressure test with the small strain data from the axial tension test, the small strain data from the axial compression test, and the higher strain data from the axial compression test. Finally, moduli were calculated from Eq [C-13] and [C-14] in Appendix C. The table theoretically indicates a dependence of the shear modulus on the axial tension or compression tests only because of the slight coupling when $\varphi \neq 0$ (the anisotropic cylinders).

The equations used for determining moduli from stiffnesses for $\varphi = 0$ (the orthotropic cylinders) offer direct insight into which moduli can be computed accurately. For $\varphi = 0$ the equations are:

$$C_{22}{}^c = \left(2h_c A_{22} - h_p A_{11}\right) \Big/ \left[\left(2h_c\right)^2 - \left(h_p\right)^2\right]$$

$$C_{11}{}^c = \left(2h_c A_{11} - h_p A_{22}\right) \Big/ \left[\left(2h_c\right)^2 - \left(h_p\right)^2\right]$$

$$C_{12}{}^c = A_{12}\big/h$$

$$C_{66}{}^c = A_{33}\big/h$$

where h_c is the thickness of a circumferential wrap layer, h_p is the thickness of the axial wrap layer, and h is the total thickness of the cylinder wall.

The moduli $C_{22}{}^c$, $C_{12}{}^c$, and $C_{66}{}^c$ are obviously insensitive to slight errors in the stiffnesses. However, the modulus perpendicular to the fibers, $C_{11}{}^c$, is small and is determined by the difference between two large numbers. This is the reason for the greatest fluctuation in data in Table 3, appearing in the Young's modulus perpendicular to the fibers. The data for shear

modulus show the greatest consistency of all the moduli, because they are obtained from a direct calculation. Young's modulus in the direction of the fibers is not quite as consistently obtained, but the fluctuations are tolerable. The data for Poisson's ratios can only be understood by recalling the definitions:

$$\text{Major Poisson's ratio} = C_{12}^{\,c} \big/ C_{11}^{\,c},$$

$$\text{Minor Poisson's ratio} = C_{12}^{\,c} \big/ C_{22}^{\,c}.$$

The great fluctuations indicated in the major Poisson's ratio results are caused by the fluctuations in the modulus perpendicular to the fibers. The data for $C_{12}^{\,c}$ are remarkably consistent (the degree of consistency of $C_{12}^{\,c}$ is indicated by the consistency of the minor Poisson's ratio column). Since $C_{12}^{\,c}$ is the quantity of interest in a shell analysis, the effect of the fluctuations in the major Poisson's ratio data is more illusory than real.

A survey of the results in Table 3 indicates no consistent ratio of the moduli obtained by using the initial axial tension data and the moduli obtained by using the initial axial compression data. However, the differences obtained by using the two sets of initial axial test data are small. Of course, greater differences in moduli are obtained by using the higher strain data of the axial compression test.

Analytical predictions of the cylinder buckling loads and a comparison with the experimentally determined loads are presented in Table 4. The analytical predictions are based on stiffnesses obtained by using the high strain axial compression data combined with the data from the internal pressure and torsion tests. In general, the buckling predictions from the characteristic equation (corresponding to a simple support solution when $\varphi = 0$) are negligibly different from the predictions of shell analysis with clamped ends specified. The magnitudes of the wave numbers encountered make this physically obvious.

When classical snap buckling occurred the experimental loads were 65 to 85% of the linear theory predictions. When local end buckles occurred, due to nonuniform clamping that warped the initial end shape of the cylinders, the experimental loads were

40 to 43% of the classical linear theory predictions. The tabulations given in Table 4 for Cylinders 6 and 7 correspond to the original 18-in. dia cylinders that experienced local end buckles. The results given for Cylinders 6a and 7a correspond to the same 18-in. dia cylinders with their damaged ends cut off. Cylinders 6a and 7a were tested with the improved clamping procedure. The two ratios tabulated for Cylinder 8 correspond to the first occurrence of the end buckles and to the final snap after more load was applied. The two 6-in. dia cylinders with $L/D \approx 5$ behaved in a manner similar to the 6-in. dia cylinders with $L/D \approx 1$. For the two long cylinders, the buckling load corresponding to $n = 2$, $m = 1$ was just slightly higher than the load corresponding to $n = 8$, $m \approx 40$. Cylinder 2 was a 6-in. dia cylinder that was initially rejected because of noticeable wetting in the composite construction. The wetting appeared to have little effect, however, on the buckling strength of the cylinder. Before the cylinders were tested, the larger diameter cylinders were expected to show a poorer comparison with linear theory than would the smaller cylinders. This was based on the increased sensitivity of the larger diameter cylinders to initial imperfections. The larger cylinders sustained remarkably high loads, however, and generally exhibited the same percentage of classical load as the smaller ones. This was due to winding the cylinders around accurately machined aluminum mandrels and, presumably, also was due to the circumferential stiffening.

The last column in Table 4 indicates the ratio of the buckling load predicted by orthotropic theory (with coupling between stretching and shear ignored) to the buckling load predicted by anisotropic theory. The effect of coupling between stretching and shear is obviously negligible for the cylinders fabricated in this study. Indeed, the cylinders were purposely designed for small coupling. The B_{16} and B_{26} elements of the [B] matrix, created by the polar winding, actually alternate in sign at each of two weave lines in a plane that is skew with respect to the longitudinal axis by the angle φ (Appendix C). If the coupling between stretching and shear were large, the nonhomogeneity of the [B] matrix would make the analysis of Cheng and Ho theoretically inapplicable. The theoretical difficulty is probably not important, however, for the following reasons:

1) If B_{16} and B_{26} were homogeneous, an arbitrary change in their sign would not affect the buckling load of a cylinder with homogeneous boundary conditions specified on right-circular ends;

2) Buckling is of a local character because of the high number of circumferential and axial waves in the buckling mode.

For these two reasons, two diametrically opposite regions on the cylinder (that are not at the weave lines) will buckle at the same applied load. If an analysis were to be made that would include the nonhomogeneity of the [B] matrix, it would probably show a slight effect from a rapidly decaying boundary layer near the two weave lines.

The effect of using initial tension moduli to calculate buckling loads, instead of the high strain axial compression data, is indicated in Table 5. Generally, the difference between the two sets of calculations is not large. The largest effect occurs in Cylinders 3 and 4. The 10 to 14% effect on Cylinders 3 and 4 is predominantly due to the difference between the moduli perpendicular to the fibers. Although the modulus perpendicular to the fibers is small, it has an important influence on D_{11}, which in turn has an important influence on the buckling strength of the cylinders[4].

There are many analytical models available for the prediction of elastic moduli of unidirectional fiber-reinforced composites. The selection of the proper model is subject to the constraint imposed by the geometric arrangement of the glass fibers within the resin matrix. Each of the layers in the cylinders fabricated for this buckling study generally have fibers that are randomly distributed. In addition, many of the fibers are contiguous because of the low resin content. For these reasons, the analytical model of S. Tsai[8] appears to be an appropriate model to compare with the moduli based on the experimental data. Young's modulus in the direction of fibers is based on the usual assumption that the fibers and the resin carry loads proportional to their stiffnesses. The models for Young's modulus perpendicular to the fibers, major Poisson's ratio, and in-plane shear modulus are constructed by linear interpolation between two extreme cases: (1) all fibers are isolated by resin; (2) all fibers are contiguous. S. Tsai's contiguity factor (C) indicates the degree to which the fibers touch. The case C = 0 indicates all fibers are isolated. The case C = 1 indicates all fibers are contiguous.

13

Table 6 provides a comparison of the experimentally determined initial tension moduli with the analytical model. The parameters used in the analytical computations are

$$E_f = 12.4 \times 10^6 \text{ psi}$$

$$\nu_f = 0.22$$

$$\gamma_f = 2.49$$

$$E_m = 0.5 \times 10^6 \text{ psi}$$

$$\nu_m = 0.35$$

$$\gamma_m = 1.22$$

$$k = 1.0,$$

where E is Young's modulus; ν is Poisson's ratio; γ is specific gravity; subscripts f and m refer to the filament and matrix, respectively; and k is a filament misalignment factor. The contiguity of the fibers is quite noticeable in the photomicrographs that were taken and has a noticeable influence on Young's modulus perpendicular to the fibers and on the shear modulus. C = 0.3 appears to be representative of the cylinders tested in this study. The contiguity factor, crude as it is, does provide a simple first approximation for the effect of contiguity of the fibers.*

The percent resin content in the composite, not the total percent resin content, is used in the theoretical model computations. The total resin contents were determined by loss of weight due to ignition of samples of the specimens taken after the tests were completed. The values of resin content in the composite material (Table 6) were determined by using the photomicrographs to estimate how much the outer resin layer contributed to the total resin content. While the difference between the two sets of resin contents is small, its influence is felt in the theoretical shear modulus. If the total percent resin content had been used, the contiguity factor C = 0.4 would have yielded a good comparison with experimental data, rather than C = 0.3. This sensitivity of shear modulus to contiguity has been noted by Ekvall[14] and can be seen in S. Tsai's results. It is an example of where a simple test can provide accurate values of modulus while an accurate theoretical prediction is difficult to achieve.

---

*For filament wound composites whose fibers are isolated by the resin matrix, the method of Hashin and Rosen[13] offers another rational method of analysis. In addition to using the same expression for the modulus in the direction of fibers, their shear modulus is identically equal to that of S. Tsai with C = 0.

V. CONCLUDING REMARKS

For cylinders with diameter to thickness ratios of 167 to 643, classical linear shell buckling theory has been found to provide a reasonable basis of comparison with the axial compression loads that a filament-wound cylinder can sustain. Still, the solutions to the following problems should be obtained:

1) A large deflection analysis for anisotropic cylinders that includes initial geometric imperfections. When design criteria are used in which the avoidance of buckling is at least a part, the layer arrangements in a filament-wound cylinder should be chosen to reduce the effect of initial imperfections. The large deflection analysis that includes the effect of initial imperfections can then be used as a design tool;

2) A large deflection analysis for anisotropic cylinders that includes the effect of boundary conditions on the prebuckling stress state. Almroth[15] has shown, for isotropic cylinders, that the classical buckling load is somewhat reduced when the effect of uniform clamping on the prebuckling state is considered;

3) Refined methods of analysis for predicting composite moduli. The effect on composite moduli of fabrication processes, a detailed study of filament contiguity, and large strain response of the resin matrix should be obtained.

15

VI. REFERENCES

1. R. E. Young: The Application Potentials of Filament-Wound Structures. Preprint of a paper presented at the 17th Annual Meeting of JANAF-ARPA, NASA, May 1961.

2. M. F. Card and J. P. Peterson: On the Instability of Orthotropic Cylinders. NASA Technical Note D-1510, Collected Papers on Instability of Shell Structures - 1962, p 297-308.

3. R. Ravenhall: Designing for Stiffness and Buckling in Filament-Wound Rocket Case Structures. Preprint of a paper presented at the AIAA Launch and Space Vehicle Shell Structures Conference, April 1963.

4. W. F. Thielemann: "New Developments in the Nonlinear Theories of the Buckling of Thin Cylindrical Shells." Aeronautics and Astronautics, Pergamon Press, 1960, p 76-119.

5. G. Gerard: Elastic and Plastic Stability of Orthotropic Cylinders. NASA Technical Note D-1510, Collected Papers on Instability of Shell Structures - 1962, p 277-295.

6. B. O. Almroth: "Postbuckling Behavior of Orthotropic Cylinders under Axial Compression." AIAA Journal, Vol 2, No. 10, October 1964, p 1795-1799.

7. E. Reissner and Y. Stavsky: "Bending and Stretching of Certain Types of Heterogeneous Aeolotropic Elastic Plates." Journal of Applied Mechanics, Vol 28, No. 3, September 1961, p 402-408.

8. S. W. Tsai: Structural Behavior of Composite Materials. Philco Corporation Report No. U-2428, January 1964.

9. S. Cheng and B. P. C. Ho: "Stability of Heterogeneous Aeolotropic Cylindrical Shells under Combined Loading." AIAA Journal, Vol 1, No. 4, April 1963, p 892-898.

10. W. Flügge: "Stresses in Shells." Springer-Verlag, Berlin, Germany, 1962.

11. L. H. Donnel: Stability of Thin-Walled Tubes under Torsion, NACA Report 479, 1933.

12. D. E. Muller: "A Method for Solving Algebraic Equations using an Automatic Computer." Math. Tables and Aides to Computation, Vol 10, October 1956, p 208-215.

13. Z. Hashin and B. W. Rosen: "The Elastic Moduli of Fiber-Reinforced Materials." Journal of Applied Mechanics, Vol 31, No. 2, June 1964, p 223-232. Also, see Errata, Vol 32, No. 1, March 1965, p 219.

14. J. C. Ekvall: "Elastic Properties of Orthotropic Monofilament Laminates." ASME Paper No. 61-AV-56. 1961.

15. B. O. Almroth: Influence of Edge Conditions on the Stability of Axially Compressed Cylindrical Shells. NASA CR-161. February 1965.

16. G. Herrmann and A. E. Armenakas: "Dynamic Behavior of Cylindrical Shells under Initial Stress." AFOSR Tech. Note 60-425, April 1960. Published in the Proceedings of the Fourth U.S. National Congress of Applied Mechanics.

17. F. B. Hildebrand: Introduction to Numerical Analysis. McGraw-Hill Book Company, Inc, New York, New York, 1956.

Table 1 Cylinder Geometry

Cylinder Number	2nd Layer Angle and Ends per Inch	Total Cylinder Length (in.)*	Average Thickness of Each Circumferential Layer (in.)	Average Total Thickness of Polar or Vertical Layer (in.)	Average Total Thickness of Cylinder (in.)	Mandrel Diameter and Maximum Deviation (in.)
1	8°49' - 400	8.08	0.0120	0.0117	0.0357	5.937 -0.000 +0.001
5	0° - 400	8.08	0.0116	0.0116	0.0348	
3	0° - 400	15.63	0.0115	0.0130	0.0360	12.623 -0.001 +0.001
4	8°34' - 400	15.63	0.0121	0.0134	0.0376	
6	0° - 408	21.73	0.0121	0.0126	0.0368	18.035 -0.003 +0.003
6a		15.18	0.0127	0.0125	0.0379	
7	8°29' - 400	21.73	0.0123	0.0126	0.0372	
7a		15.12	0.0121	0.0128	0.0370	
8	0° - 416	28.25	0.0130	0.0125	0.0385	23.868 -0.005 +0.002
9	8°33' - 400	28:25	0.0121	0.0130	0.0372	
11	0° - 400	31.91	0.0119	0.0116	0.0354	5.955 -0.000 +0.003
12	2°56' - 400	31.91	0.0115	0.0118	0.0348	
2	0° - 400	8.08	0.0117	0.0112	0.0346	5.937 -0.000 +0.001

*Total length between clamping rings is 1.40 in. less.

Table 2 Test Results

Load-Strain Slopes and Buckling Loads

Cylinder No.	Nominal Diameter (in.)	Nominal L/D	Winding Type	Internal Pressure				Torsion		Gages Used for Internal Pressure Axial Slopes
				Pre-loaded	psi/microinch/in.			Pre-loaded	(Principal Strain used) in.-lb/microinch/in.	
					Axial	Circumferential				
2	6	1	Vertical		0.176	0.0911		Yes	5.78	All axial
5	6	1	Vertical	Yes	0.167	0.1024		Yes	5.68	All axial
1	6	1	Polar		0.154	0.0942		Yes	5.71	All axial
11	6	5	Vertical	Yes	0.162	0.0882		Yes	6.20	2 and 3
12	6	5	Polar		0.167	0.0946			6.06	2 and 3
3	12	1	Vertical	Yes	0.0847	0.0466			27.6	2 and 3
4	12	1	Polar	Yes	0.0912	0.0470			28.6	2 and 3
6	18	1	Vertical	Yes	0.0572	0.0329		Yes	53.1	2 and 3
6a	18	3/4		Yes	0.0552	0.0327		Yes	53.2	All axial
7	18	1	Polar		0.0550	0.0299			51.7	2 and 3
7a	18	3/4		Yes	0.0580	0.0319		Yes	52.3	All axial
8	24	1	Vertical		0.0356	0.0236			106.7	2 and 3
9	24	1	Polar	Yes	0.0436	0.0247		Yes	89.4	2 and 3

Cylinder No.	Tension			Compression-Buckling							Gages Used for Tension and Compression Axial Slopes
	Pre-Loaded	lb/microinch/in.		Pre-loaded to 2000 lb	lb/microinch/in.				Failure Load (lb)	Location of Buckle	
		Axial	Circumferential		Axial		Circumferential				
					Initial	Final	Initial	Final			
2		3.68	-28.5	Yes	3.56	3.17	-26.4	-23.0	14,800	Minus	All axial
5	Yes	3.45	-23.7	Yes	3.37	3.41	-24.7	-24.7	16,120	Minus	All axial
1	Yes	3.30	-22.7	Yes	3.48	3.23	-23.5	-21.3	14,020	Minus	All axial
11	Yes	3.52	-29.3		3.61	3.39	-26.9	-26.9	16,210	Plus	2 and 3
12		3.78	-21.2		3.56	3.57	-25.2	-26.9	15,710	Plus	2 and 3
3		7.72	-59.3		7.70	7.14	-59.8	-55.5	13,430	Plus	2 and 3
4		8.23	-56.7		8.56	7.21	-58.3	-58.3	14,830	Plus	2 and 3
6		10.90	-75.7		12.30	11.44	-76.9	-76.9	9,250	Plus	2 and 3
6a	Yes	10.86	-75.7	Yes	11.18	10.67	-95.2	-95.2	14,050	Plus	All axial
7		10.30	-79.2		10.36	10.67	-93.1	-93.1	9,170	Minus	2 and 3
7a	Yes	10.75	-70.0	Yes	10.35	11.21	-71.9	-71.9	17,350	Plus	All axial
8		14.26	-110.0	Yes	13.78	13.36	-115.4	-115.4	{8,980 / 10,780}	Plus	2 and 3
9		14.56	-113.6		15.01	14.75	-116.6	-116.6	14,980	Plus	2, 3, 11, 12

Table 3 Moduli of Cylinders

Cylinder Number	Axial Test Slopes Used	Young's Modulus in Direction of Fibers, 10^6 psi	Young's Modulus Perpendicular to Fibers, 10^6 psi	Major Poisson's Ratio	Minor Poisson's Ratio	Shear Modulus, 10^6 psi*
1	Initial Tension	8.86	3.09	0.32	0.11	
	Initial Compression	8.64	3.61	0.28	0.12	1.39
	Final Compression	8.85	2.93	0.35	0.12	
5	Initial Tension	10.13	2.77	0.41	0.11	
	Initial Compression	10.37	2.45	0.43	0.10	1.46
	Final Compression	10.30	2.59	0.41	0.10	
3	Initial Tension	10.00	2.72	0.35	0.10	
	Initial Compression	10.03	2.68	0.36	0.10	1.52
	Final Compression	10.36	1.79	0.52	0.09	
4	Initial Tension	9.10	3.59	0.28	0.11	
	Initial Compression	8.85	4.08	0.25	0.11	1.47
	Final Compression	10.01	1.98	0.43	0.09	
6	Initial Tension	9.34	3.02	0.34	0.11	
	Initial Compression	8.52	4.50	0.25	0.13	1.41
	Final Compression	9.04	3.58	0.30	0.12	
6a	Initial Tension	8.80	3.14	0.32	0.11	
	Initial Compression	9.02	3.28	0.26	0.09	1.37
	Final Compression	9.28	2.78	0.29	0.09	
7	Initial Tension	8.33	3.22	0.26	0.10	1.32
	Initial Compression	8.52	3.18	0.22	0.08	1.32
	Final Compression	7.70	4.69	0.17	0.11	1.31
7a	Initial Tension	8.88	3.20	0.32	0.12	
	Initial Compression	9.17	2.74	0.35	0.10	1.34
	Final Compression	8.67	3.66	0.28	0.12	
8	Initial Tension	8.13	3.34	0.26	0.11	
	Initial Compression	8.40	2.96	0.27	0.09	1.54
	Final Compression	8.56	2.66	0.29	0.09	
9	Initial Tension	9.42	3.06	0.29	0.09	
	Initial Compression	9.26	3.40	0.26	0.10	1.29
	Final Compression	9.37	3.20	0.27	0.09	
11	Initial Tension	8.38	3.76	0.22	0.10	
	Initial Compression	8.11	4.09	0.22	0.11	1.56
	Final Compression	8.48	3.41	0.25	0.10	
12	Initial Tension	8.50	4.33	0.29	0.15	
	Initial Compression	9.31	3.39	0.30	0.11	1.54
	Final Compression	9.41	3.37	0.29	0.10	
2	Initial Tension	8.61	4.24	0.22	0.11	
	Initial Compression	8.69	3.92	0.25	0.11	1.49
	Final Compression	9.11	2.79	0.35	0.11	

*Independent of axial test slope for orthotropic cylinders.

Table 4 Cylinder Buckling Loads

Cylinder Number	$\frac{L}{D}$	$\frac{D}{h}$	θ (deg)	Solution from Characteristic Equation			Solution for Clamped Ends		Experimental Load (lb)	$\left(\dfrac{\text{Experimental Load}}{\text{Solution for Clamped Ends}}\right)$	$\left(\dfrac{\text{Orthotropic Theory, } [B] \equiv 0}{\text{Anisotropic Theory, } [B] \neq 0}\right)$
				n	m	Load (lb)	n	Load (lb)			
1	1.118	167	8.82	8	9	19,064	8	19,152	14,020	0.73	1.016
5	1.119	171	0.0	8	10	18,973	8	19,046	16,120	0.85	
3	1.124	352	0.0	10	18	18,943	10	18,977	13,430	0.71	
4	1.124	336	8.57	10	17	20,029	10	20,073	14,830	0.74	1.028
6	1.125	491	0.0	14	14	21,759	14	21,800	9,250*	0.42	
6a	0.762	477	0.0	13	11	21,151	13	21,215	14,050†	0.66	
7	1.125	486	8.48	14	12	21,434	14	21,490	9,170*	0.43	1.008
7a	0.759	488	8.48	13	10	21,257	13	21,329	17,350†	0.81	1.016
8	1.123	621	0.0	15	20	22,323	15	22,344	$\left\{\begin{matrix}8,980\\10,780\end{matrix}\right\}$ *	$\left\{\begin{matrix}0.40\\0.48\end{matrix}\right\}$	
9	1.123	643	8.55	15	17	20,507	15	20,528	14,980	0.73	1.021
11	5.095	169	0.0	8	39	19,944	8	19,948	16,210	0.81	
12	5.095	172	2.93	8	41	19,777	8	19,780	15,710	0.79	1.006
2	1.119	173	0.0	8	10	18,479	8	18,542	14,800	0.80	

*Load corresponding to local end buckling.
†Load on shortened cylinder with improved clamping procedure.

Table 5 Effect of Method Used for Determining Moduli
on Theoretical Buckling Loads

Cylinder Number	$\left(\dfrac{\begin{matrix}\text{Buckling Load Using}\\\text{Initial Tension Moduli}\end{matrix}}{\begin{matrix}\text{Buckling Load Using}\\\text{Final Compression Moduli}\end{matrix}}\right)$
1	1.007
5	1.016
3	1.095
4	1.143
6	0.970
6a	1.034
7	0.938
7a	0.974
8	1.051
9	0.992
11	1.015
12	1.060
2	1.070

Table 6 Comparison of Tension Moduli With an Analytical Model

Method Used	Cylinder No.	Total Resin Content (Percent by Weight)	Resin Content in Composite (Percent by Weight)	E_{22}^c Young's Modulus in Direction of Fibers, 10^6 psi	E_{11}^c Young's Modulus Perpendicular to Fibers, 10^6 psi	ν_{12} Major Poisson's Ratio	C_{66}^c Shear Modulus, 10^6 psi
Experiment	1	20.4	18.2	8.85	3.09	0.32	1.39
Tsai C = 0.4				8.68	3.05	0.24	1.62
C = 0.3					2.75	0.25	1.43
C = 0.2					2.45	0.25	1.23
C = 0.0					1.86	0.26	0.84
Experiment	2	20.4	17.0	8.61	4.24	0.22	1.49
Tsai C = 0.4				8.90	3.21	0.24	1.69
C = 0.3					2.90	0.25	1.49
C = 0.2					2.59	0.25	1.29
C = 0.0					1.97	0.25	0.89
Experiment	3	18.7	16.2	9.79	3.16	0.32	1.52
Tsai C = 0.4				9.04	3.32	0.24	1.74
C = 0.3					3.00	0.24	1.54
C = 0.2					2.68	0.25	1.34
C = 0.0					2.04	0.25	0.93
Experiment	4	19.3	18.7	9.10	3.59	0.28	1.47
Tsai C = 0.4				8.60	2.99	0.25	1.60
C = 0.3					2.70	0.25	1.40
C = 0.2					2.41	0.25	1.21
C = 0.0					1.82	0.26	0.82
Experiment	5	19.3	17.4	10.13	2.77	0.41	1.46
Tsai C = 0.4				8.83	3.16	0.24	1.67
C = 0.3					2.85	0.25	1.47
C = 0.2					2.54	0.25	1.27
C = 0.0					1.93	0.25	0.88
Experiment	6	21.3	19.0	9.34	3.02	0.34	1.41
	6a			8.80	3.14	0.32	1.37
	7			8.33	3.22	0.26	1.32
	7a			8.88	3.20	0.32	1.34
Tsai C = 0.4				8.55	2.95	0.25	1.58
C = 0.3					2.66	0.25	1.39
C = 0.2					2.37	0.25	1.20
C = 0.0					1.80	0.26	0.81
Experiment	8	21.3	†	8.13	3.34	0.26	1.54
	9	20.4	†	9.42	3.06	0.29	1.29
Experiment	11	19.4	16.6	8.38	3.76	0.22	1.56
Tsai C = 0.4				8.96	3.25	0.24	1.71
C = 0.3					2.94	0.25	1.51
C = 0.2					2.63	0.25	1.31
C = 0.0					2.00	0.25	0.91
Experiment	12	19.4	16.4	8.50	4.33	0.29	1.54
Tsai C = 0.4				8.99	3.28	0.24	1.73
C = 0.3					2.97	0.25	1.52
C = 0.2					2.65	0.25	1.32
C = 0.0					2.02	0.25	0.92

†The photomicrographs for Cylinders 8 and 9 were adequate to provide composite layer thickness data but were not adequate to distinguish the surface resin layer thickness.
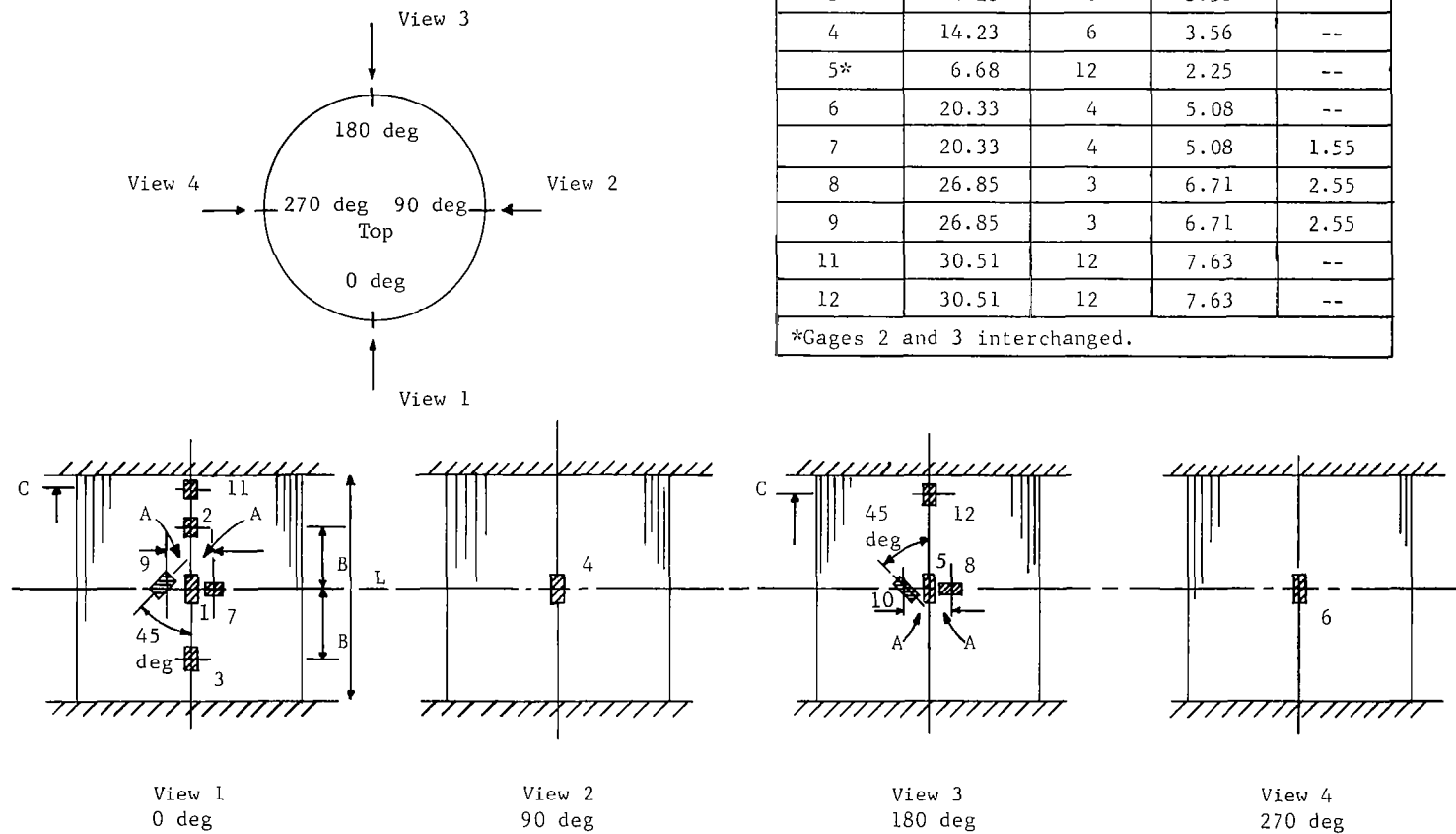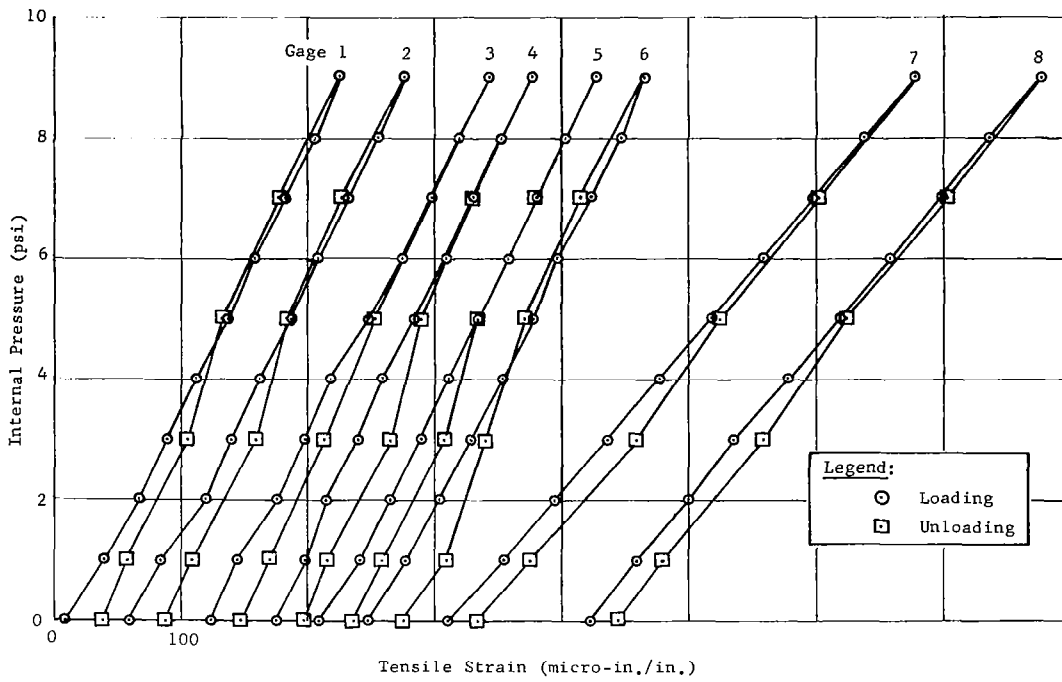
Cylinder	L (in.)	A (deg)	B (in.)	C (in.)
1*	6.68	12	2.25	--
2	6.68	15	--	--
3	14.23	6	3.56	--
4	14.23	6	3.56	--
5*	6.68	12	2.25	--
6	20.33	4	5.08	--
7	20.33	4	5.08	1.55
8	26.85	3	6.71	2.55
9	26.85	3	6.71	2.55
11	30.51	12	7.63	--
12	30.51	12	7.63	--
*Gages 2 and 3 interchanged.				

Fig. 1 Strain Gage Locations

Fig. 2 Cylinder 9, Internal Pressure vs Strain
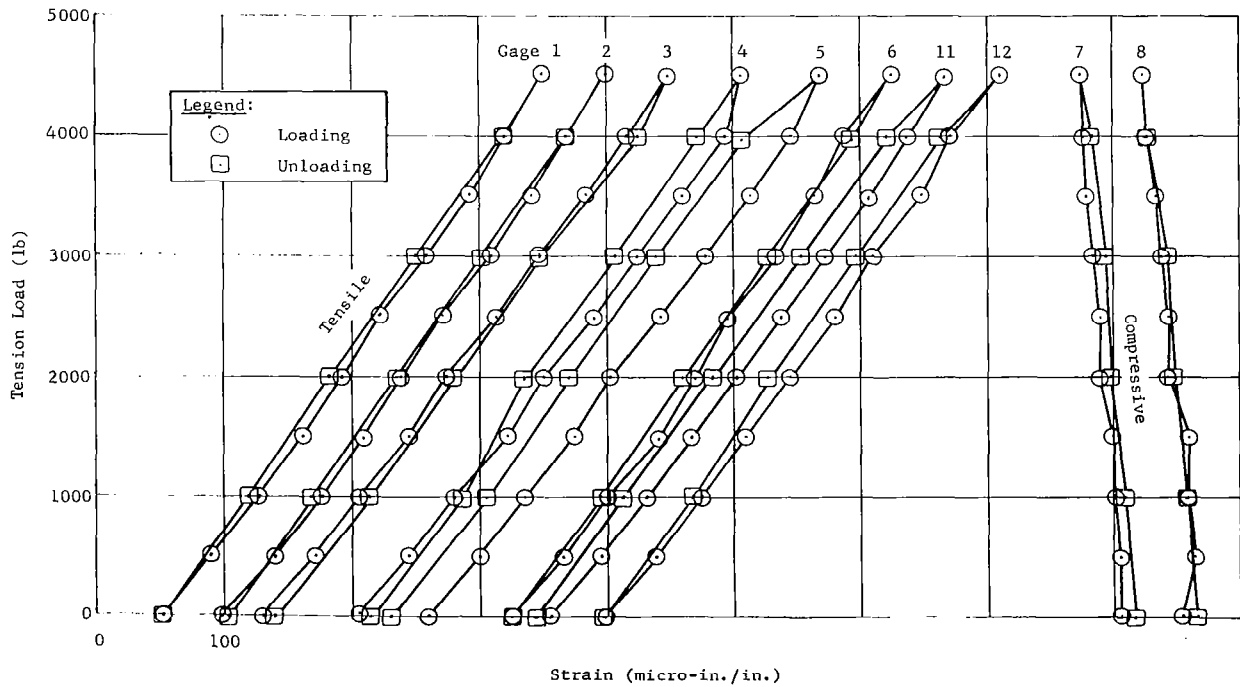
Fig. 3 Cylinder 9, Tension Load vs Strain
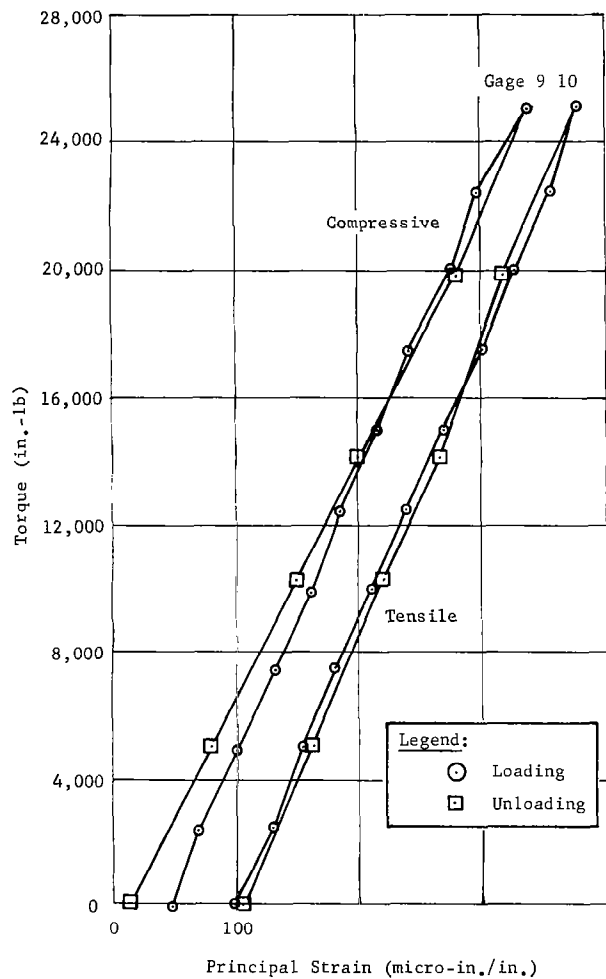
Fig. 4 Cylinder 9, Torque vs Strain
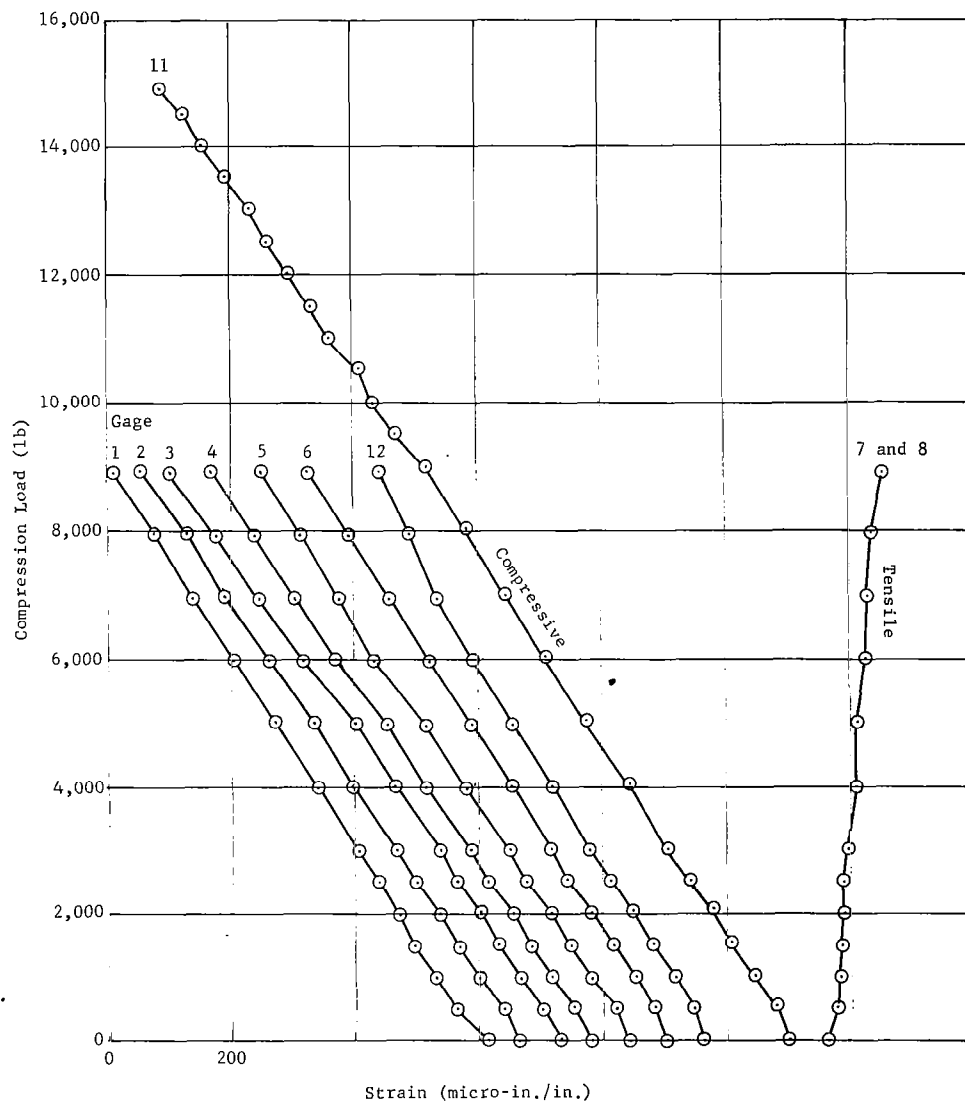
Fig. 5 Cylinder 9, Compression Load vs Strain
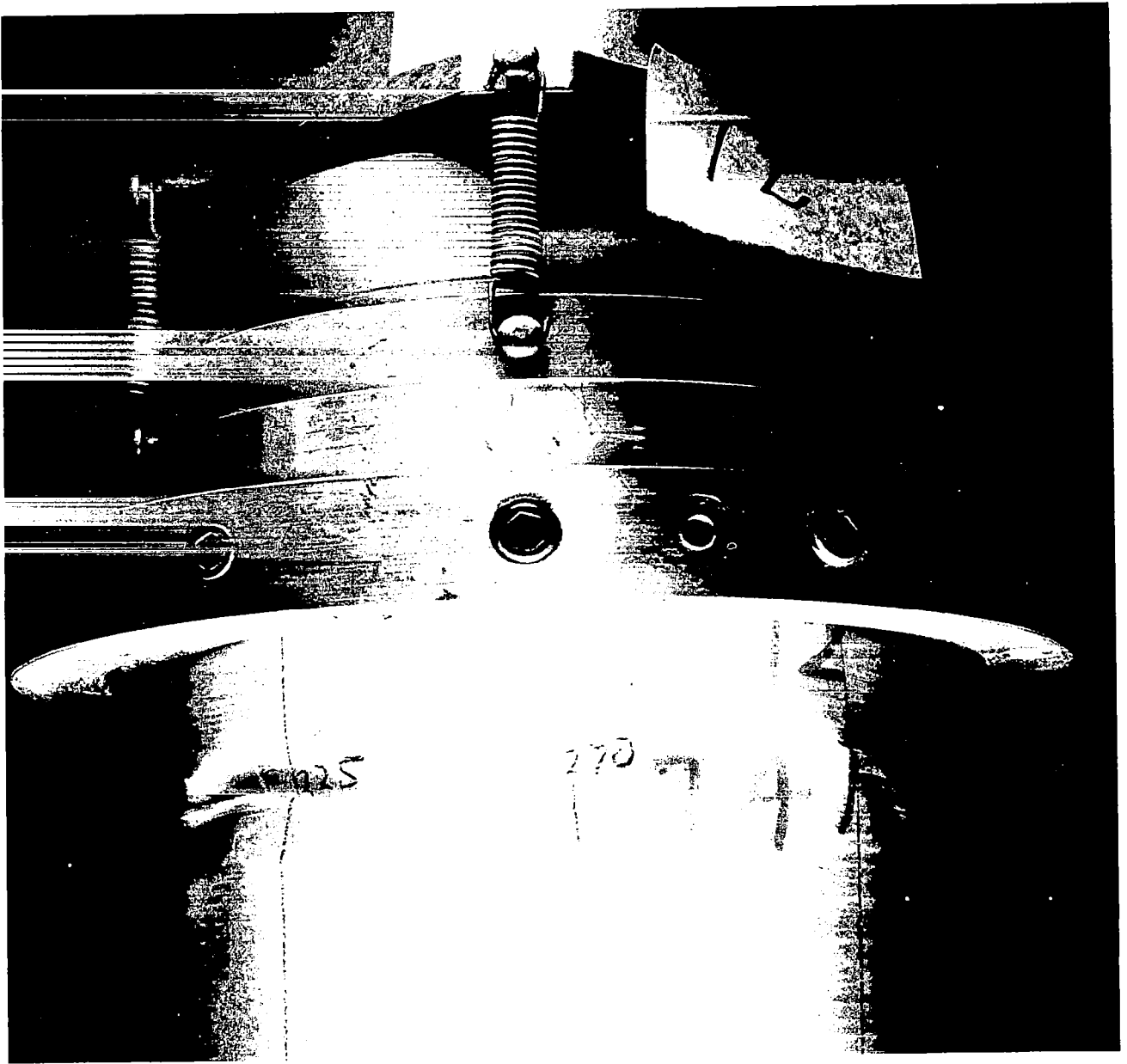
Fig. 6   Cylinder 12 (6-in. dia) in Postbuckled State
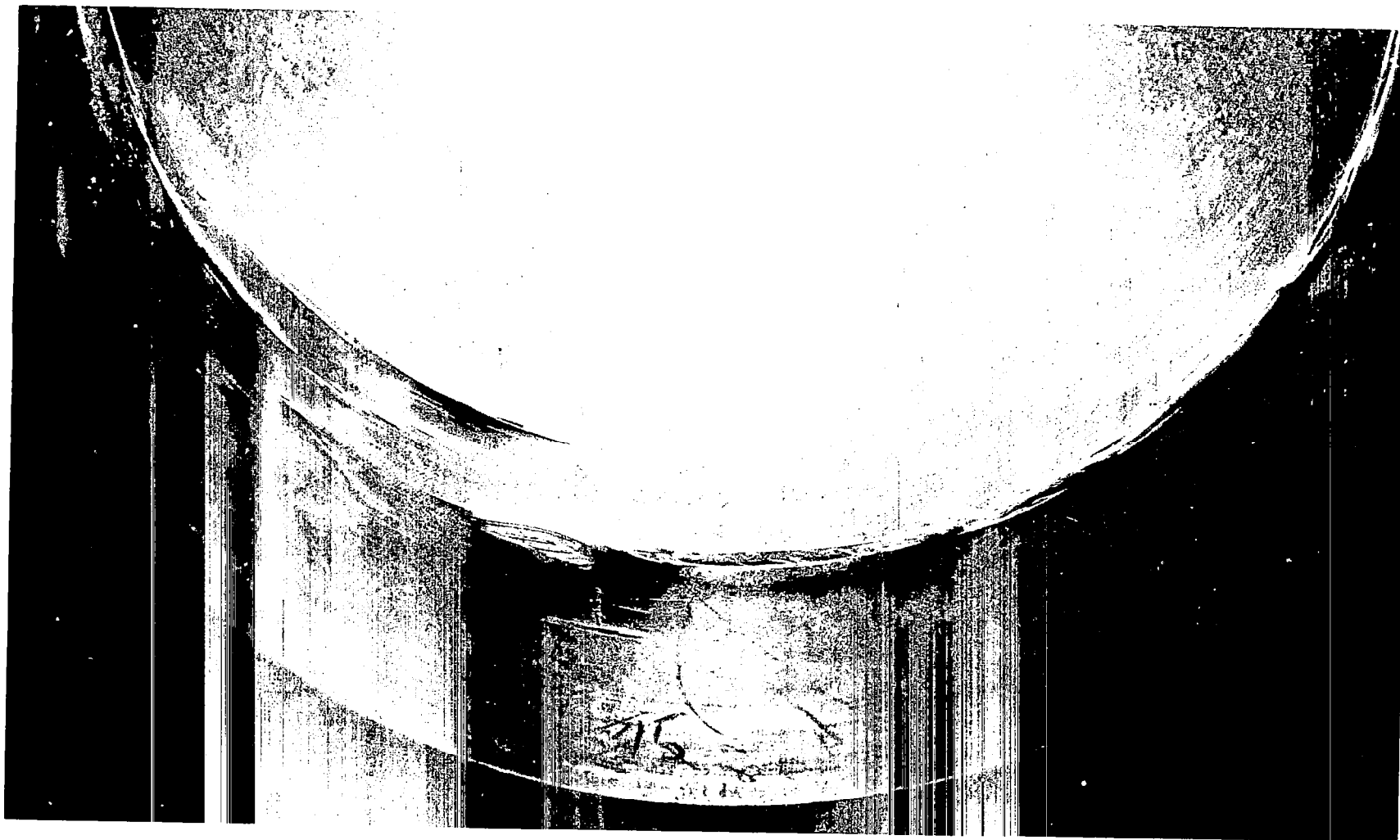
Fig. 7 Cylinder 12, View of Inside after Test

Fig. 8 Cylinder 1 (6-in. dia) after Test

29
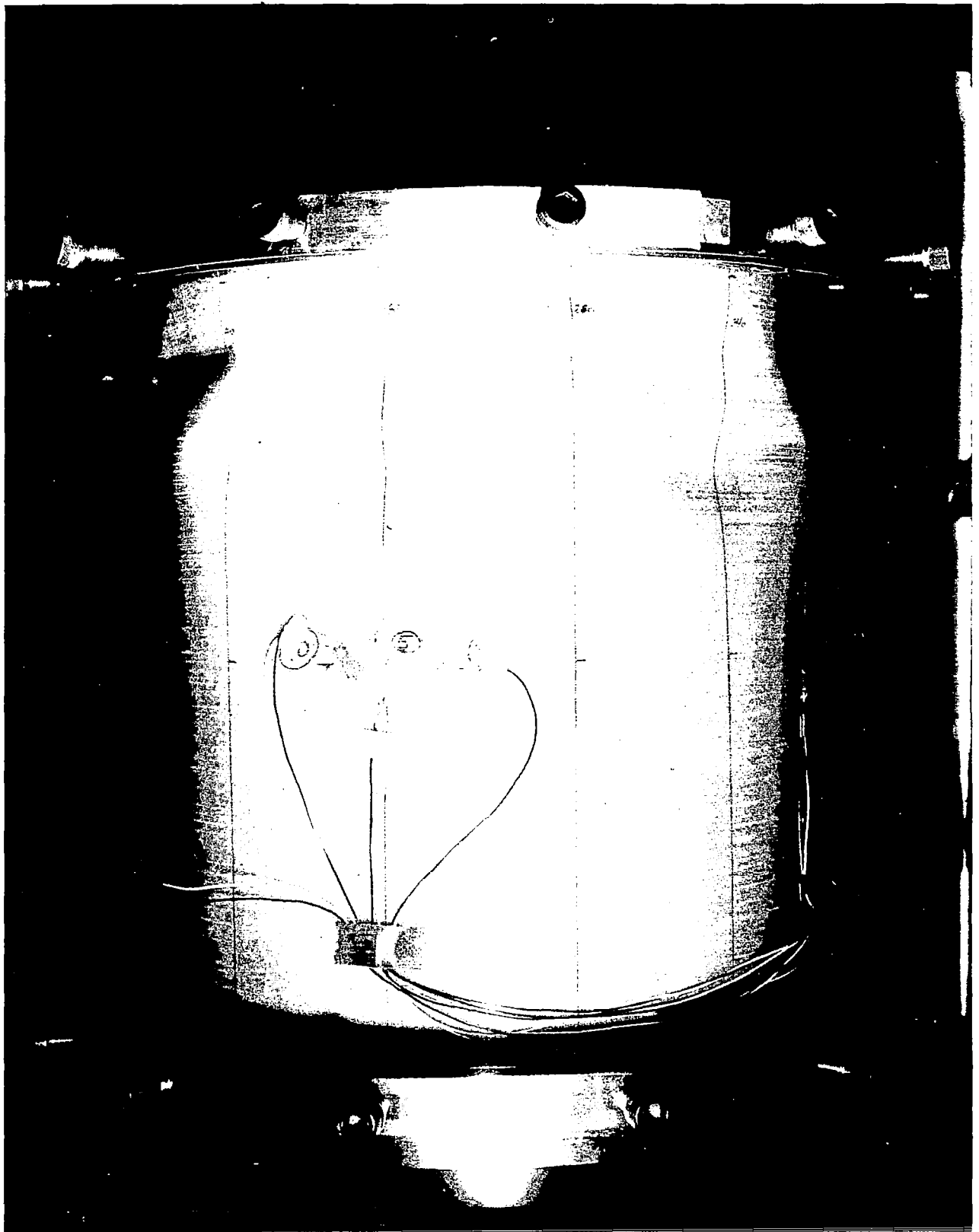
Fig. 9   Cylinder 4   (12-in.dia) in Postbuckled State

Fig. 10   Cylinder 6   (18-in.dia) in Postbuckled State
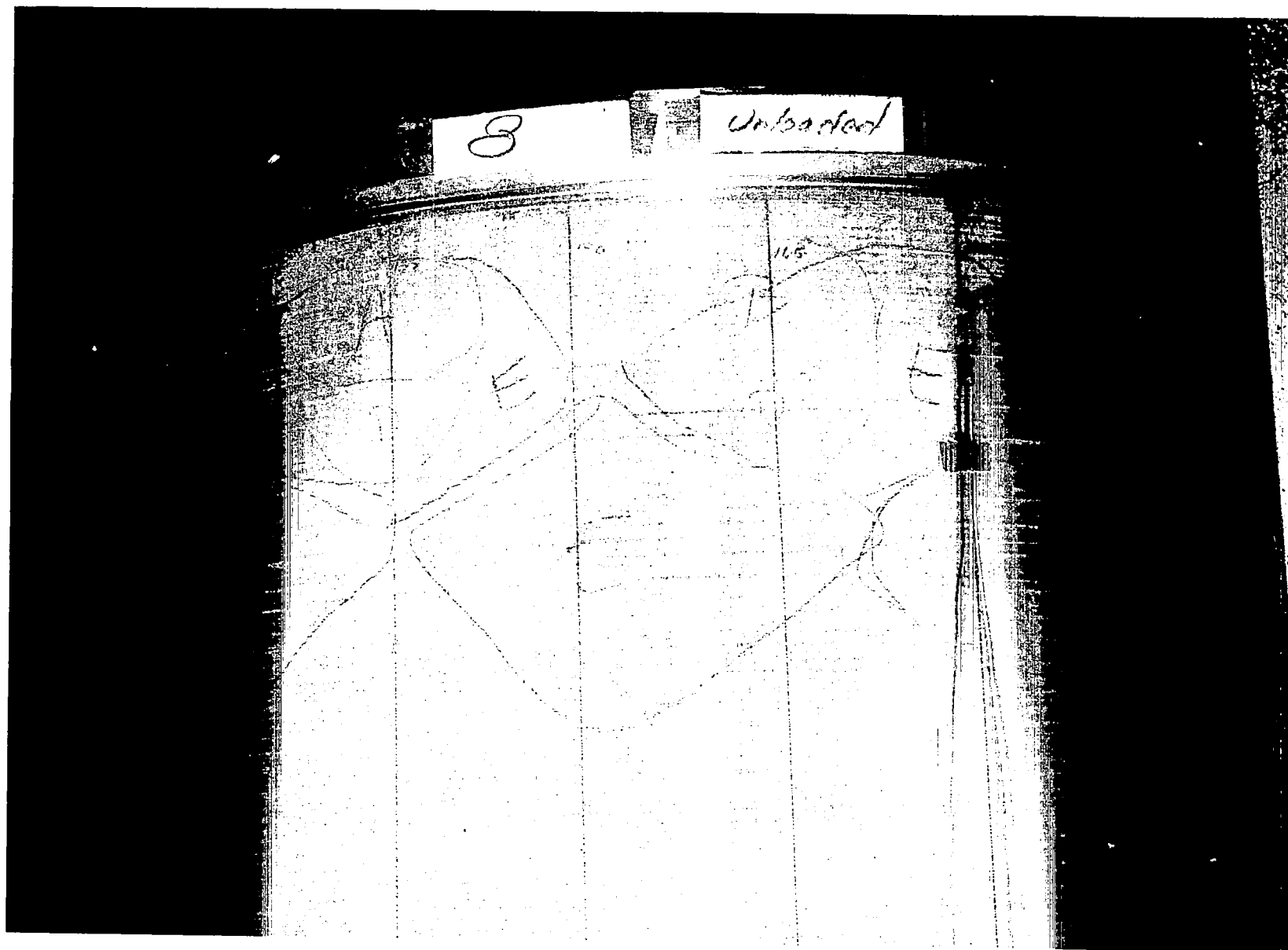
Fig. 11   Cylinder 8 (24-in. dia) after Test
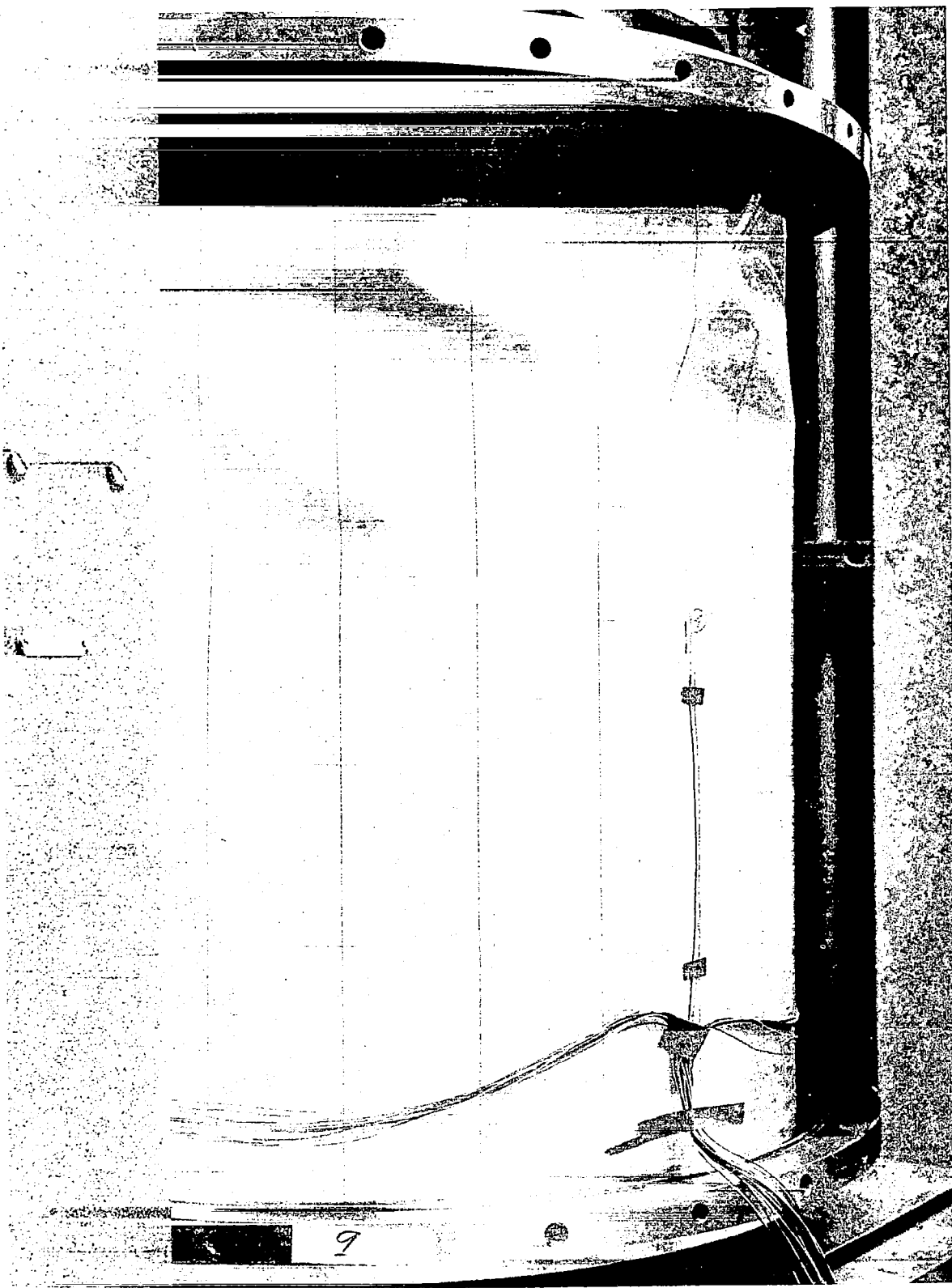
Fig. 12 Cylinder 9 (24-in. dia) in Postbuckled State
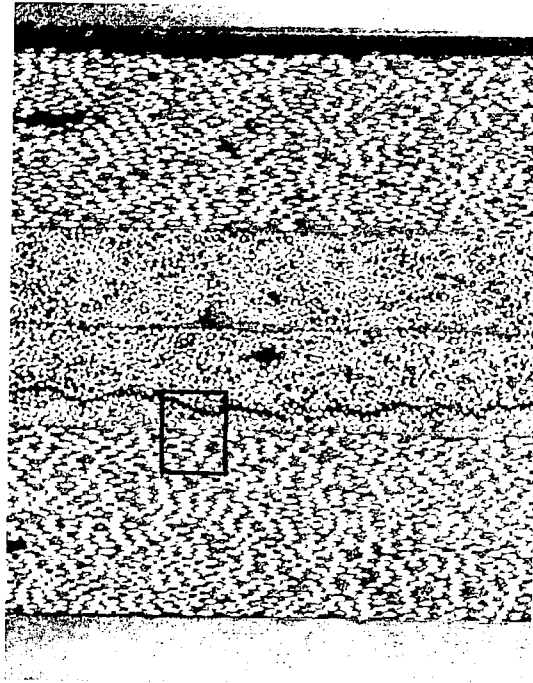
Fig. 13   Cylinder 9, Photomicrograph of Cylinder Wall
           (Taken at an angle of 19°30' with respect
           to the axis of the cylinder, 80X)

Fig. 14   Cylinder 9, Detail of Crack Shown in Fig. 13
           (700X)
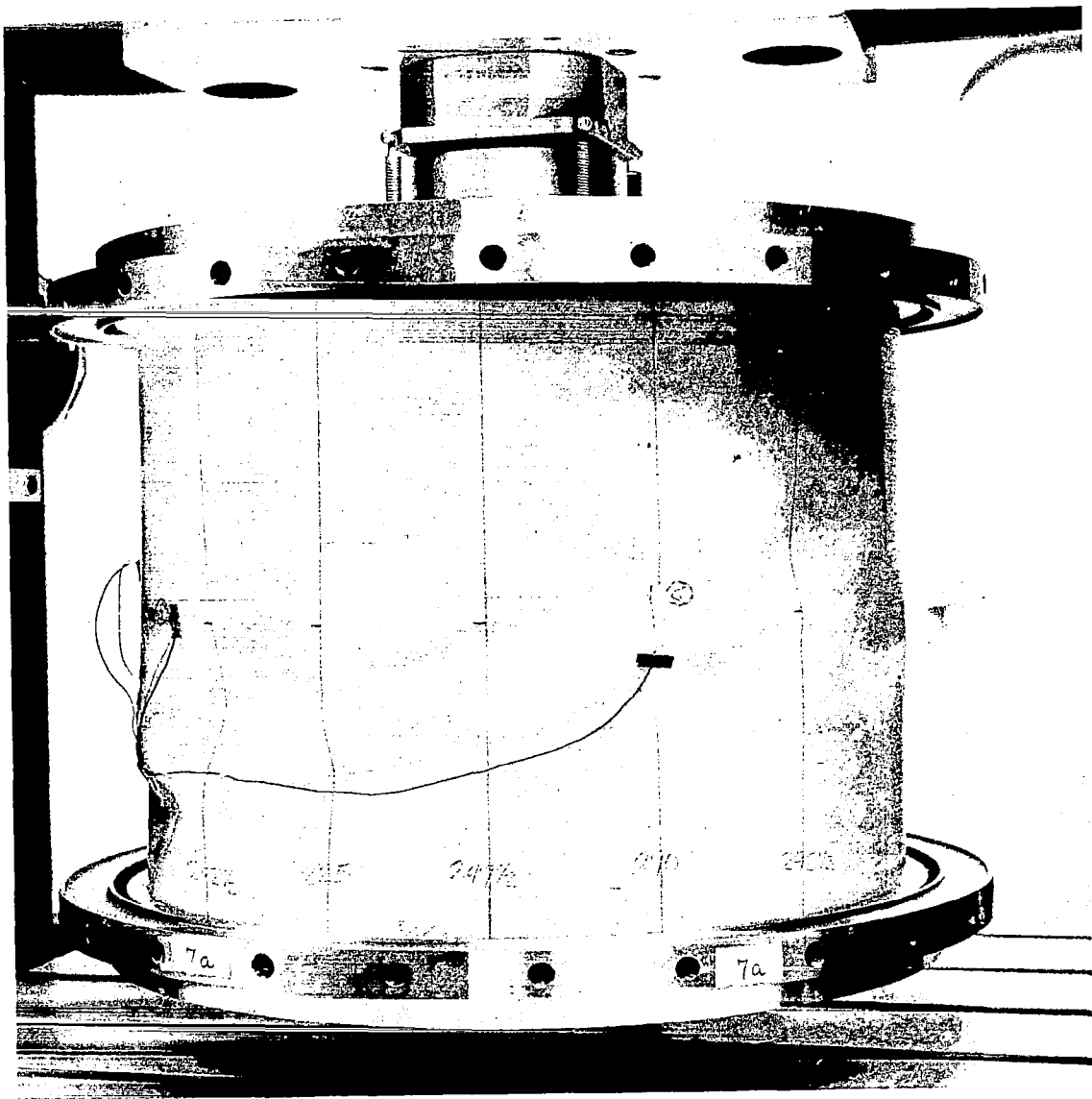
Fig. 15   Cylinder 7a (Shortened 18-in. dia Cylinder) in Postbuckled State

APPENDIX A

FABRICATION OF CYLINDERS

A single lot of pre-impregnated fiberglas roving was obtained
from U.S. Polymeric Chemical Co. for the fabrication of all the
cylinders. This material was 20 end, S994 roving with an HTS finish,
and was impregnated with an epoxy resin system designated EF 787
by U.S. Polymeric Chemical Co.

All cylinders were wrapped with a roving tension of 10 lb, and
consisted of three layers of material. The first and third layers
were wrapped circumferentially and contained 400 ends per inch roving.
The middle layer parameters were systematically varied and are listed
in Table 1. The nominal wall thickness of all cylindrical specimens
was 0.036 in. All cylinders were cured in the same oven, using a
cam that resulted in the following cure cycle: 6 hr from 200 to
350°F plus 16 hr at 350°F. Following cure, the specimens were cut
to the length shown in Table 1. The layer thicknesses in Table 1
are averages of values taken from four photomicrographs of cross-
sections cut from the cylinder after testing. The values are
exclusive of a thin resin layer that exists on the outer surface
of each of the cylinders due to compaction of the rovings.

SOLUTION OF EQUATIONS OF EQUILIBRIUM

.

Appendix B describes the analysis used to obtain the buckling strengths of clamped filament-wound cylinders under axial compression.

<u>Stress Equations of Equilibrium</u> - A cylindrical shell of constant thickness h and mean radius R is referred to a modified cylindrical system of coordinates x, θ, and z as indicated in Fig. B-1; x is measured along the axis of the shell, θ along the circumference, and z in the direction perpendicular to the middle surface.

The linear stress equations of equilibrium[10] in terms of the notation of this report are:

$$\frac{\partial N_{xx}}{\partial x} + \frac{1}{R}\frac{\partial N_{\theta x}}{\partial \theta} + N^i_{xx}\frac{\partial^2 u}{\partial x^2} + \frac{N^i_{\theta\theta}}{R^2}\frac{\partial^2 u}{\partial \theta^2} - \frac{N^i_{\theta\theta}}{R}\frac{\partial w}{\partial x} + 2\frac{N^i_{x\theta}}{R}\frac{\partial^2 u}{\partial x\partial\theta} = 0; \qquad [B-1]$$

$$\frac{1}{R}\frac{\partial N_{\theta\theta}}{\partial \theta} + \frac{\partial N_{x\theta}}{\partial x} + \frac{1}{R^2}\frac{\partial M_{\theta\theta}}{\partial \theta} + \frac{1}{R}\frac{\partial M_{x\theta}}{\partial x} + N^i_{xx}\frac{\partial^2 v}{\partial x^2} +$$

$$+ \frac{N^i_{\theta\theta}}{R^2}\frac{\partial}{\partial \theta}\left(w + \frac{\partial v}{\partial \theta}\right) + 2\frac{N^i_{x\theta}}{R}\frac{\partial}{\partial x}\left(w + \frac{\partial v}{\partial \theta}\right) = 0; \qquad [B-2]$$

$$\frac{\partial^2 M_{xx}}{\partial x^2} + \frac{1}{R^2}\frac{\partial^2 M_{\theta\theta}}{\partial \theta^2} + \frac{1}{R}\frac{\partial^2 M_{\theta x}}{\partial\theta\partial x} + \frac{1}{R}\frac{\partial^2 M_{x\theta}}{\partial\theta\partial x} - \frac{N_{\theta\theta}}{R} + N^i_{xx}\frac{\partial^2 w}{\partial x^2} +$$

$$+ \frac{N^i_{\theta\theta}}{R}\left(\frac{\partial u}{\partial x} - \frac{1}{R}\frac{\partial v}{\partial \theta} + \frac{1}{R}\frac{\partial^2 w}{\partial \theta^2}\right) + 2\frac{N^i_{x\theta}}{R}\frac{\partial}{\partial x}\left(\frac{\partial w}{\partial \theta} - v\right) = 0; \qquad [B-3]$$
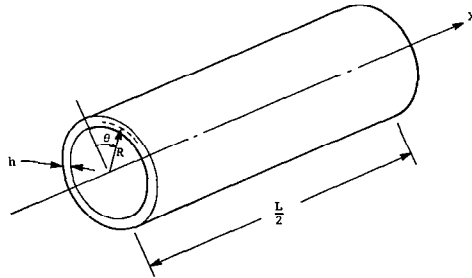

Fig. B-1 Cylindrical Coordinate System for Composite Shell

where

$$N_{xx} = \int_{-h/2}^{h/2} \sigma_{xx}\left(1 + \frac{z}{R}\right)dz, \quad M_{xx} = \int_{-h/2}^{h/2} \sigma_{xx}\left(1 + \frac{z}{R}\right)zdz,$$

$$N_{\theta\theta} = \int_{-h/2}^{h/2} \sigma_{\theta\theta}dz, \qquad M_{\theta\theta} = \int_{-h/2}^{h/2} \sigma_{\theta\theta}zdz,$$

$$N_{x\theta} = \int_{-h/2}^{h/2} \sigma_{x\theta}\left(1 + \frac{z}{R}\right)dz, \quad M_{x\theta} = \int_{-h/2}^{h/2} \sigma_{x\theta}\left(1 + \frac{z}{R}\right)zdz,$$

$$N_{\theta x} = \int_{-h/2}^{h/2} \sigma_{x\theta}dz, \qquad M_{\theta x} = \int_{-h/2}^{h/2} \sigma_{x\theta}zdz.$$

[B-4]

The superscript i refers to the initial stress state; stress re-
sultants and moments without superscripts represent the additional
stresses that occur with buckling; u, v, and w are the displacements
in the axial, circumferential, and radial directions, respectively,
which arise due to buckling. The cylinders to be considered are
thin (h/2R $\ll$ 1). This has been used extensively to reduce the
number of initial stress terms possible.[16] The initial stress re-
sultants used for axial loading are:

$$N_{xx}^i = -\frac{LOAD}{\pi D}, \quad N_{\theta\theta}^i = 0, \quad N_{x\theta}^i = 0.$$

Constitutive Equations - The anisotropic stress-strain relation-
ship for a cylinder in a state of plane stress is

$$\begin{bmatrix} \sigma_{xx} \\ \sigma_{\theta\theta} \\ \sigma_{x\theta} \end{bmatrix} = \begin{bmatrix} C_{11} & C_{12} & C_{16} \\ C_{12} & C_{22} & C_{26} \\ C_{16} & C_{26} & C_{66} \end{bmatrix} \bullet \begin{bmatrix} e_{xx} \\ e_{\theta\theta} \\ e_{x\theta} \end{bmatrix}$$

[B-5]

with the Flügge strain expressions given by

$$
\begin{bmatrix} e_{xx} \\ e_{\theta\theta} \\ e_{x\theta} \end{bmatrix} = \begin{bmatrix} \epsilon^o_{xx} + z\kappa_{xx} \\ \epsilon^o_{\theta\theta} + z\left(1 - \frac{z}{R}\right)\kappa_{\theta\theta} \\ \left(1 + \frac{z^2}{2R^2}\right)\epsilon^o_{x\theta} + z\left(1 - \frac{z}{2R}\right)\kappa_{x\theta} \end{bmatrix}
$$

[B-6]

$$
\left.
\begin{array}{ll}
\epsilon^o_{xx} = \dfrac{\partial u}{\partial x}, & \kappa_{xx} = -\dfrac{\partial^2 w}{\partial x^2} \\[3mm]
\epsilon^o_{\theta\theta} = \dfrac{w}{R} + \dfrac{1}{R}\dfrac{\partial v}{\partial \theta}, & \kappa_{\theta\theta} = -\dfrac{1}{R^2}\left(w + \dfrac{\partial^2 w}{\partial \theta^2}\right) \\[3mm]
\epsilon^o_{x\theta} = \dfrac{1}{R}\dfrac{\partial u}{\partial \theta} + \dfrac{\partial v}{\partial x}, & \kappa_{x\theta} = -\dfrac{2}{R}\left(\dfrac{\partial^2 w}{\partial \theta \partial x} + \dfrac{1}{2R}\dfrac{\partial u}{\partial \theta} - \dfrac{1}{2}\dfrac{\partial v}{\partial x}\right).
\end{array}
\right\}
$$

[B-7]

The constitutive equations for the cylinder are obtained by substituting Eq [B-5] and [B-6] into [B-4]. The expressions are given by Cheng and Ho[9] and are repeated here.

$$
\begin{bmatrix} N_{xx} \\ N_{\theta\theta} \\ N_{x\theta} \\ N_{\theta x} \\ M_{xx} \\ M_{\theta\theta} \\ M_{x\theta} \\ M_{\theta x} \end{bmatrix} =
\begin{bmatrix}
\left(A_{11} + \frac{B_{11}}{R}\right) & \left(A_{12} + \frac{B_{12}}{R}\right) & \left(A_{16} + \frac{B_{16}}{R} + \frac{D_{16}}{2R^2}\right) & \left(B_{11} + \frac{D_{11}}{R}\right) & B_{12} & \left(B_{16} + \frac{D_{16}}{2R}\right) \\
A_{12} & A_{22} & \left(A_{26} + \frac{D_{26}}{2R^2}\right) & B_{12} & \left(B_{22} - \frac{D_{22}}{R}\right) & \left(B_{26} - \frac{D_{26}}{2R}\right) \\
\left(A_{16} + \frac{B_{16}}{R}\right) & \left(A_{26} + \frac{B_{26}}{R}\right) & \left(A_{66} + \frac{B_{66}}{R} + \frac{D_{66}}{2R^2}\right) & \left(B_{16} + \frac{D_{16}}{R}\right) & B_{26} & \left(B_{66} + \frac{D_{66}}{2R}\right) \\
A_{16} & A_{26} & \left(A_{66} + \frac{D_{66}}{2R^2}\right) & B_{16} & \left(B_{26} - \frac{D_{26}}{R}\right) & \left(B_{66} - \frac{D_{66}}{2R}\right) \\
\left(B_{11} + \frac{D_{11}}{R}\right) & \left(B_{12} + \frac{D_{12}}{R}\right) & \left(B_{16} + \frac{D_{16}}{R}\right) & D_{11} & D_{12} & D_{16} \\
B_{12} & B_{22} & B_{26} & D_{12} & D_{22} & D_{26} \\
\left(B_{16} + \frac{D_{16}}{R}\right) & \left(B_{26} + \frac{D_{26}}{R}\right) & \left(B_{66} + \frac{D_{66}}{R}\right) & D_{16} & D_{26} & D_{66} \\
B_{16} & B_{26} & B_{66} & D_{16} & D_{26} & D_{66}
\end{bmatrix}
\bullet
\begin{bmatrix} e^o_{xx} \\ e^o_{\theta\theta} \\ e^o_{x\theta} \\ \kappa_{xx} \\ \kappa_{\theta\theta} \\ \kappa_{x\theta} \end{bmatrix}
$$

with [A], [B], and [D] defined by

$$[A] = \int_{-h/2}^{h/2} [C]\ dz$$

$$[B] = \int_{-h/2}^{h/2} [C]\ zdz \qquad\qquad\qquad \rbrace \qquad [B\text{-}9]$$

$$[D] = \int_{-h/2}^{h/2} [C]\ z^2dz.$$

For the cylinders considered in this study, the stiffness matrices reduce to the forms

$$[A] = \begin{bmatrix} A_{11} & A_{12} & 0 \\ A_{12} & A_{22} & 0 \\ 0 & 0 & A_{66} \end{bmatrix}, \quad [B] = \begin{bmatrix} 0 & 0 & B_{16} \\ 0 & 0 & B_{26} \\ B_{16} & B_{26} & 0 \end{bmatrix}, \quad [D] = \begin{bmatrix} D_{11} & D_{12} & 0 \\ D_{12} & D_{22} & 0 \\ 0 & 0 & D_{66} \end{bmatrix}.$$

See Eq [C-3], [C-4], and [C-5] in Appendix C.

  Characteristic Equation - The displacement equations of equilibrium are obtained by substituting Eq [B-8] and [B-7] into Eq [B-1] thru [B-3]. The substitution of displacements of the form

$$u = A\ \sin\!\left(\frac{\lambda x}{R} + n\theta\right)$$

$$v = B\ \sin\!\left(\frac{\lambda x}{R} + n\theta\right)$$

$$w = C\ \cos\!\left(\frac{\lambda x}{R} + n\theta\right)$$

into the equations of equilibrium yields the characteristic determinant

$$\begin{vmatrix} a_{11} & a_{12} & a_{13} \\ a_{12} & a_{22} & a_{23} \\ a_{13} & a_{23} & a_{33} \end{vmatrix} = 0 \qquad\qquad [B\text{-}10]$$

with

$$a_{11} = \left[\left(A_{11} + \frac{B_{11}}{R} + N_{xx}^i\right)\lambda^2 + \left(A_{66} - \frac{B_{66}}{R} + \frac{D_{66}}{R^2} + N_{\theta\theta}^i\right)n^2 + 2\left(A_{16} + N_{x\theta}^i\right)\lambda n\right]$$

$$a_{12} = \left[\left(A_{16} + \frac{2B_{16}}{R} + \frac{D_{16}}{R^2}\right)\lambda^2 + A_{26}n^2 + \left(A_{12} + \frac{B_{12}}{R} + A_{66} + \frac{B_{66}}{R}\right)\lambda n\right]$$

$$a_{13} = \left[\left(\frac{B_{11}}{R} + \frac{D_{11}}{R^2}\right)\lambda^3 + \left(A_{12} - N_{\theta\theta}^i\right)\lambda + \left(A_{26} - \frac{B_{26}}{R} + \frac{D_{26}}{R^2}\right)n + \right.$$
$$\left. + \left(\frac{3B_{16}}{R} + \frac{D_{16}}{R^2}\right)\lambda^2 n + \left(\frac{2B_{66}}{R} + \frac{B_{12}}{R} - \frac{D_{66}}{R^2}\right)\lambda n^2 + \left(\frac{B_{26}}{R} - \frac{D_{26}}{R^2}\right)n^3\right]$$

$$a_{22} = \left[\left(A_{22} + \frac{B_{22}}{R} + N_{\theta\theta}^i\right)n^2 + 2\left(A_{26} + 2\frac{B_{26}}{R} + \frac{D_{26}}{R^2} + N_{x\theta}^i\right)\lambda n + \right.$$
$$\left. + \left(A_{66} + 3\frac{B_{66}}{R} + 3\frac{D_{66}}{R^2} + N_{xx}^i\right)\lambda^2\right]$$

$$a_{23} = \left[\left(A_{22} + N_{\theta\theta}^i\right)n + \left(\frac{B_{12}}{R} + \frac{D_{12}}{R^2} + \frac{2B_{66}}{R} + \frac{3D_{66}}{R^2}\right)\lambda^2 n + \frac{B_{22}}{R}n^3 + \right.$$
$$\left. + \left(3\frac{B_{26}}{R} + 2\frac{D_{26}}{R^2}\right)\lambda n^2 + \left(A_{26} + \frac{B_{26}}{R} + 2N_{x\theta}^i\right)\lambda + \left(\frac{B_{16}}{R} + 2\frac{D_{16}}{R^2}\right)\lambda^3\right]$$

$$a_{33} = \left[\frac{D_{11}}{R^2}\lambda^4 + 4\frac{D_{16}}{R^2}\lambda^3 n + 2\left(\frac{D_{12}}{R^2} + 2\frac{D_{66}}{R^2}\right)\lambda^2 n^2 + 4\frac{D_{26}}{R^2}\lambda n^3 + \right.$$
$$+ \frac{D_{22}}{R^2}\left(n^2 - 1\right)^2 + \left(2\frac{B_{12}}{R} + N_{xx}^i\right)\lambda^2 + \left(2\frac{B_{22}}{R} + N_{\theta\theta}^i\right)n^2 +$$
$$\left. + 2\left(2\frac{B_{26}}{R} - \frac{D_{26}}{R^2} + N_{x\theta}^i\right)\lambda n + A_{22} - \frac{B_{22}}{R}\right]$$

and $n = 0, 1, 2, 3, \ldots$.

41

If $\lambda = m\pi R/L$, $m = 1, 2, 3 \ldots$, the solutions correspond to boundary conditions that are determined by the trigonometric form of the assumed solutions. The solutions to be found by this procedure are obtained by expanding the characteristic determinant into the form

$$P_0\left(N_{xx}^i\right)^3 + P_1\left(N_{xx}^i\right)^2 + P_2 N_{xx}^i + P_3 = 0. \qquad [B-11]$$

Equation [B-11] is solved by the Newton-Raphson procedure.[17] The first approximation for N_{xx}^i is given by

$$N_{xx}^i \approx - P_3/P_2.$$

The iteration is completed when

$$\left| \frac{\left(N_{xx}^i\right)_{j+1} - \left(N_{xx}^i\right)_j}{\left(N_{xx}^i\right)_{j+1}} \right| \leq 1 \times 10^{-6}.$$

The calculations are performed by an IBM 1620 computer. For a given value of n the axial buckling load is printed for m = 1 through a maximum specified value of m. The minimum buckling load for the given value of n is also printed. The procedure is then repeated, with n increased by unity, until the maximum specified value for n is achieved. Generally, a maximum of two iterations is required for each N_{xx}^i. The case n = 0 sometimes requires five iterations.

Effect of Boundary Conditions - The solution for arbitrary boundary conditions uses displacements of the form:

$$u = \sum_{k=1}^{8} A_k \sin\left(\frac{\lambda_k x}{R} + n\theta\right)$$

$$v = \sum_{k=1}^{8} B_k \sin\left(\frac{\lambda_k x}{R} + n\theta\right)$$

$$w = \sum_{k=1}^{8} C_k \cos\left(\frac{\lambda_k x}{R} + n\theta\right) \qquad [B-12]$$

where λ_k represents the roots of the eighth order polynomial equation obtained by expanding the characteristic determinant Eq [B-10] in powers of λ. Since each root satisfies the characteristic equation, the displacements corresponding to each root can be superimposed.

Because the coefficients of the polynomial equation are real, a complex root must be accompanied by a root that is its complex conjugate. Consider the two roots

$$\lambda_k = \lambda_{rk} + i\lambda_{ik}$$

$$\lambda_{k+1} = \lambda_{rk} - i\lambda_{ik}.$$

Since the displacements are real, we have

$$C_k = C_{rk} + iC_{ik}$$

$$C_{k+1} = C_{rk} - iC_{ik}.$$

The expansion of the k and k + 1 components of w in Eq [B-12] in terms of its real and imaginary parts yields the real sum

$$w_k + w_{k+1} = \left(2C_{rk}\zeta_{2k} + 2C_{ik}\zeta_{1k}\right) \cos n\theta$$

$$+ \left(-2C_{rk}\zeta_{3k} + 2C_{ik}\zeta_{4k}\right) \sin n\theta$$

where

$$\zeta_{1k} = \sin\left(\lambda_{rk} \frac{x}{R}\right) \sinh\left(\lambda_{ik} \frac{x}{R}\right)$$

$$\zeta_{2k} = \cos\left(\lambda_{rk} \frac{x}{R}\right) \cosh\left(\lambda_{ik} \frac{x}{R}\right)$$

$$\zeta_{3k} = \sin\left(\lambda_{rk} \frac{x}{R}\right) \cosh\left(\lambda_{ik} \frac{x}{R}\right)$$

$$\zeta_{4k} = \cos\left(\lambda_{rk} \frac{x}{R}\right) \sinh\left(\lambda_{ik} \frac{x}{R}\right)$$

The u and v displacements are treated in a similar manner. The modal amplitudes A_k and B_k are found in terms of C_k from the equations of equilibrium. Let

$$A_k = \left(f^A_{rk} + i f^A_{ik} \right) C_k$$

$$B_k = \left(f^B_{rk} + i f^B_{ik} \right) C_k$$

then

$$u_k + u_{k+1} = \left(2C_{rk} U^A_{cr} - 2C_{ik} U^A_{ci} \right) \cos n\theta$$

$$+ \left(2C_{rk} U^A_{sr} - 2C_{ik} U^A_{si} \right) \sin n\theta$$

where

$$U_{cr} = f^A_{rk} \zeta_{3k} - f^A_{ik} \zeta_{4k}$$

$$U^A_{ci} = f^A_{ik} \zeta_{3k} + f^A_{rk} \zeta_{4k}$$

$$U^A_{sr} = f^A_{rk} \zeta_{2k} + f^A_{ik} \zeta_{1k}$$

$$U^A_{si} = f^A_{ik} \zeta_{2k} - f^A_{rk} \zeta_{1k}.$$

The sum $v_k + v_{k+1}$ is obtained by replacing superscript A by superscript B. Slopes and stress resultants are obtained by suitable differentiations of the displacements. When two real roots occur, instead of a pair of complex conjugate roots, they are represented in the summations for the total deflections by the coefficients of $2C_{rk}$ with $2C_{ik} = 0$.

All of the ingredients required for satisfying boundary conditions are now available. The clamped conditions, corresponding to the experiments, are $u = v = w = \frac{\partial w}{\partial x} = 0$ at $x = \pm L/2$. Setting the coefficients of $\cos n\theta$ and $\sin n\theta$ equal to zero, one arrives at eight simultaneous homogeneous algebraic equations. For given geometric and stiffness properties of the cylinder, the lowest value of N_{xx}^i that sets the determinant of the coefficients of $2C_{rk}$ and $2C_{ik}$ equal to zero is the load per unit of circumferential length that is required to buckle the cylinder.

APPENDIX C

DETERMINATION OF STIFFNESSES AND MODULI

Appendix C describes the analysis used to obtain the stiffnesses and moduli of filament-wound cylinders from suitable test data. The tests required are internal pressure, axial tension or axial compression, and torsion.

Transformation Equations for Composite Moduli – The composite modulus matrix for a filament-wound structure in a state of plane stress has an orthotropic form when referred to axes along, and perpendicular to, the fiber direction. Let x', y', z' denote such a system of axes, with the fibers directed along x'. The orthotropic modulus matrix C' can be written as

$$[C'] = \begin{bmatrix} C'_{11} & C'_{12} & 0 \\ C'_{12} & C'_{22} & 0 \\ 0 & 0 & C'_{66} \end{bmatrix}.$$

An in-plane rotation to a new coordinate system (x,y,z) is accomplished by

$$\begin{bmatrix} x \\ y \\ z \end{bmatrix} = \begin{bmatrix} \cos\varphi & -\sin\varphi & 0 \\ \sin\varphi & \cos\varphi & 0 \\ 0 & 0 & 1 \end{bmatrix} \begin{bmatrix} x' \\ y' \\ z' \end{bmatrix}$$

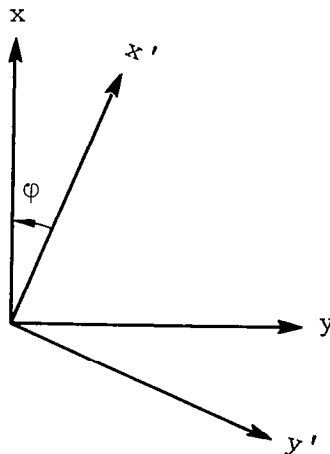where φ is the angle of rotation shown in Fig. C-1.

Fig. C-1 Transformation Axes for Composite Moduli

Since [C'] transforms according to the standard rules for a fourth rank tensor, its representation in the new coordinate system is given by*

$$[C] = \begin{bmatrix} C_{11} & C_{12} & C_{16} \\ C_{12} & C_{22} & C_{26} \\ C_{16} & C_{26} & C_{66} \end{bmatrix}$$

where

$$C_{11} = c^4 C'_{11} + 2\left(C'_{12} + 2C'_{66}\right) s^2 c^2 + s^4 C'_{22}$$

$$C_{12} = c^2 s^2 \left(C'_{11} + C'_{22} - 4C'_{66}\right) + \left(c^4 + s^4\right) C'_{12}$$

$$C_{16} = cs \left[\left(c^2 C'_{11} - s^2 C'_{22}\right) - \left(c^2 - s^2\right)\left(C'_{12} + 2C'_{66}\right)\right]$$

$$C_{22} = s^4 C'_{11} + 2c^2 s^2 \left(C'_{12} + 2C'_{66}\right) + c^4 C'_{22} \qquad [C-1]$$

$$C_{26} = cs \left[\left(s^2 C'_{11} - c^2 C'_{22}\right) + \left(c^2 - s^2\right)\left(C'_{12} + 2C'_{66}\right)\right]$$

$$C_{66} = c^2 s^2 \left(C'_{11} + C'_{22} - 2C'_{12}\right) + \left(c^2 - s^2\right)^2 C'_{66}$$

and

$$c = \cos \varphi$$

$$s = \sin \varphi.$$

Constitutive Equations - The stress-strain relationship for a polar half-layer referred to the longitudinal and circumferential directions is

$$\begin{bmatrix} \sigma_{xx} \\ \sigma_{\theta\theta} \\ \sigma_{x\theta} \end{bmatrix} = \begin{bmatrix} C_{11} & C_{12} & sig_j(z)C_{16} \\ C_{12} & C_{22} & sig_j(z)C_{26} \\ sig_j(z)C_{16} & sig_j(z)C_{26} & C_{66} \end{bmatrix} \cdot \begin{bmatrix} e_{xx} \\ e_{\theta\theta} \\ e_{x\theta} \end{bmatrix} \qquad [C-2]$$

---

*The compact representation of the fourth rank tensor components C'_{ijkl} by matrix notation C'_{mn} is only a convenience. To transform the components of the moduli to other axes it is necessary to use the complete tensor notation.

where,

j refers to the jth polar half-layer,

$sig_j(z) = \pm 1$ for polar angle $= \pm\varphi$.

The wall of each cylinder fabricated for this study is composed of three layers. The inner and outer layers are circumferential windings of equal thickness h_c; the middle layer is a polar winding with two half-layers wound at angle of wrap $\pm\varphi$ and total thickness h_p. The in-plane, coupling, and bending stiffness matrices [A], [B], and [D] are obtained by applying the [C] matrix in Eq [C-2] to Eq [B-9]. The result is

$$[A] = \int_{-h/2}^{h/2} [C]\, dz = 2h_c\left[C^c\right] + h_p \begin{bmatrix} C_{11}^P & C_{12}^P & 0 \\ C_{12}^P & C_{22}^P & 0 \\ 0 & 0 & C_{66}^P \end{bmatrix} \qquad [C\text{-}3]$$

$$[B] = \int_{-h/2}^{h/2} [C]\, z\,dz = \frac{h_p^2}{4} \begin{bmatrix} 0 & 0 & {}^-_+C_{16}^P \\ 0 & 0 & {}^-_+C_{26}^P \\ {}^-_+C_{16}^P & {}^-_+C_{26}^P & 0 \end{bmatrix} \qquad [C\text{-}4]$$

$$[D] = \int_{-h/2}^{h/2} [C]\, z^2\,dz = \frac{1}{12}\left\{ \begin{aligned} &\left[C^c\right]\left(\left(h_p + 2h_c\right)^3 - h_p^3\right) + \\ &+ h_p^3 \begin{bmatrix} C_{11}^P & C_{12}^P & 0 \\ C_{12}^P & C_{22}^P & 0 \\ 0 & 0 & C_{66}^P \end{bmatrix} \end{aligned} \right\} \qquad [C\text{-}5]$$

48

with

$$[C^c] = \begin{bmatrix} C_{11}^c & C_{12}^c & 0 \\ C_{12}^c & C_{22}^c & 0 \\ 0 & 0 & C_{66}^c \end{bmatrix} \qquad [C-6]$$

The superscripts c and p indicate the modulus matrices for the circumferential layer and the polar layer, respectively.

The elements of $[C^p]$ are computed from Eq [C-1] with

$$C_{11}' = C_{22}^c = \text{composite modulus in the fiber direction}$$

$$C_{12}' = C_{12}^c = \text{composite modulus representing Poisson's ratio effect}$$

$$C_{22}' = C_{11}^c = \text{composite modulus perpendicular to the fibers}$$

$$C_{66}' = C_{66}^c = \text{composite shear modulus}$$

$$[C-7]$$

Hence, there are only four independent moduli C_{22}^c, C_{12}^c, C_{11}^c, C_{66}^c to be determined.

It is assumed that the quality of the construction of the cylinder is such that each layer has the same uniform properties when referred to the direction of winding. This can be qualitatively confirmed for an individual cylinder by using a light source to illuminate the wall of the cylinder. The transparency of a thin filament-wound cylinder permits a visual inspection of the uniformity of construction. The lack of a complete bond between resin and fibers is simply detected by black streaks where wetting has occurred.

The choice of the sign in [B] depends on which side of the polar wrap is considered. While the sign convention chosen for φ is arbitrary (hence the sign convention of B_{16}, B_{26} is arbitrary), the existence of the two different signs is not arbitrary. The sign in [B] alternates at each of two diametrically opposite weave lines in the polar wrap. The two weave lines are parallel to each other in a plane that intersects the center of the cylinder and is skew with respect to the longitudinal axis by the angle φ.

In order to understand why the weave occurs, one must understand how a polar wrap is wound around a mandrel. The plane in which the fibers are wound is kept constant while the mandrel is continuously rotated until a complete rotation of 360 deg is achieved. Figures C-2 thru C-7 illustrate three phases of the winding sequence.[*] Figures C-2 and C-3 are front and rear views, respectively, of the first polar encirclement of roving around the mandrel. Notice that when the roving is referenced with respect to the local surface of the mandrel two diametrically opposite fibers in the roving are oriented at angles that are equal to each other in magnitude but are opposite in sign. Figures C-4 and C-5 represent front and rear[†] views of the rovings on the mandrel after the mandrel has rotated 180 deg. One can see the beginning of the overlapping of rovings. Also, by considering only those parts of the rovings that are in contact with the surface of the mandrel, one can see that the half-layer on the left side of Fig. C-4 has an orientation that is opposite to the orientation of the half-layer on the right side of Fig. C-4. The same is true for the rear view shown in Fig. C-5. Figures C-6 and C-7 are front and rear views of roving on the mandrel just before the mandrel has completed its 360 deg rotation (hence, just before the two outside half-layers and the two weave lines are completed). A detailed view of a weave "line" in Cylinder 1 is given by the photomicrograph in Fig. C-8. The rovings in the outer polar half layer are seen to gradually turn into what is called the inner polar half layer. Also, the transition length required for this is seen to be of the order of magnitude of the thickness of the shell.

_____

[*]A black-coated mandrel and gaps between rovings are used in Fig. C-2 thru C-7 for illustration purposes. The cylinders fabricated for the buckling study were wound around cylindrical aluminum mandrels and the rovings were laid adjacent to each other.

[†]The front views in Fig. C-2, C-4, and C-6 are taken from the same position. Similarly, the rear views in Fig. C-3, C-5, and C-7 are taken from the same rear position, directly opposite the front view.

<u>Determination of Stiffness and Moduli</u> - The simplified forms
of the stiffness matrices given by Eq [C-3], [C-4], and [C-5] reduce
the constitutive relations Eq [B-8] to

$$
\left.\begin{aligned}
N_{xx} &= A_{11}\epsilon^{o}_{xx} + A_{12}\epsilon^{o}_{\theta\theta} + \frac{B_{16}}{R}\epsilon^{o}_{x\theta} + \frac{D_{11}}{R}\kappa_{xx} + B_{16}\kappa_{x\theta} \\[2ex]
N_{\theta\theta} &= A_{12}\epsilon^{o}_{xx} + A_{22}\epsilon^{o}_{\theta\theta} - \frac{D_{22}}{R}\kappa_{\theta\theta} + B_{26}\kappa_{x\theta} \\[2ex]
N_{x\theta} &= \frac{B_{16}}{R}\epsilon^{o}_{xx} + \frac{B_{26}}{R}\epsilon^{o}_{\theta\theta} + \left(A_{66} + \frac{D_{66}}{2R^{2}}\right)\epsilon^{o}_{x\theta} + \\[2ex]
&\quad + B_{16}\kappa_{xx} + B_{26}\kappa_{\theta\theta} + \frac{D_{66}}{2R}\kappa_{x\theta}
\end{aligned}\right\} \qquad \text{[C-8]}
$$

with similar expressions for $N_{\theta x}$ and the bending moments.

For the moment, assume [B] is homogeneous. Since N_{xx} = constant,
$N_{\theta\theta}$ = constant, and $N_{x\theta}$ = constant in the three tests considered,
there can be no changes in displacements with respect to θ. If all
strain data are obtained at the midsection of the cylinder the
curvature due to restraint of the cylinder ends can be neglected
and thus:

$$
\epsilon^{o}_{xx} = \frac{\partial u}{\partial x}, \quad \kappa_{xx} = -\frac{\partial^{2}w}{\partial x^{2}} = 0
$$

$$
\epsilon^{o}_{\theta\theta} = \frac{w}{R}, \quad \kappa_{\theta\theta} = -\frac{w}{R^{2}} = -\frac{\epsilon^{o}_{\theta\theta}}{R}
$$

$$
\epsilon^{o}_{x\theta} = \frac{\partial v}{\partial x}, \quad \kappa_{x\theta} = \frac{1}{R}\frac{\partial v}{\partial x} = \frac{\epsilon^{o}_{x\theta}}{R}.
$$

Eq [C-8] reduces to

$$N_{xx} = A_{11}\epsilon^o_{xx} + A_{12}\epsilon^o_{\theta\theta} + \frac{2B_{16}}{R}\epsilon^o_{x\theta}$$

$$N_{\theta\theta} = A_{12}\epsilon^o_{xx} + \left(A_{22} + \frac{D_{22}}{R^2}\right)\epsilon^o_{\theta\theta} + \frac{B_{26}}{R}\epsilon^o_{x\theta} \qquad \text{[C-9]}$$

$$N_{x\theta} = \frac{B_{16}}{R}\epsilon^o_{xx} + 0 + \left(A_{66} + \frac{D_{66}}{R^2}\right)\epsilon^o_{x\theta}$$

Now consider longitudinal tension and internal pressure applied to the shell. With no restraint provided to rotation at the ends, $N_{x\theta} = 0$. Therefore,

$$\epsilon^o_{x\theta} = \frac{-\dfrac{B_{16}}{R}\epsilon^o_{xx}}{\left(A_{66} + \dfrac{D_{66}}{R^2}\right)}$$

and

$$N_{xx} = A_{11}\left[1 - \frac{2\left(\dfrac{B_{16}}{R}\right)^2}{A_{11}\left(A_{66} + \dfrac{D_{66}}{R^2}\right)}\right]\epsilon^o_{xx} + A_{12}\epsilon^o_{\theta\theta}$$

$$N_{\theta\theta} = A_{12}\left[1 - \frac{\dfrac{B_{26}}{R} \cdot \dfrac{B_{16}}{R}}{A_{12}\left(A_{66} + \dfrac{D_{66}}{R^2}\right)}\right]\epsilon^o_{xx} + \left(A_{22} + \frac{D_{22}}{R^2}\right)\epsilon^o_{\theta\theta}.$$

The expressions in brackets differ from unity by terms of order $(h/R)^2$. Because of the thinness of the shells, the difference can be effectively neglected. The constitutive equations used for determining A_{11}, A_{12}, and A_{22} for orthotropic cylinders ($\varphi = 0$) are therefore equally valid for the anisotropic cylinders ($\varphi \neq 0$).

52

The in-plane stiffnesses $\left(A_{11}, A_{12}, \text{ and } A_{22}\right)$ are determined by first applying uniform tensile loads to the ends of the cylinder $N_{xx} = \text{Load}/\pi D$, $N_{\theta\theta} = 0$ and measuring the principal strains $\left(\epsilon_{xx}^{o}\right)_{T}$ and $\left(\epsilon_{\theta\theta}^{o}\right)_{T}$. After the tension test is completed, internal pressure p is applied $\left(N_{\theta\theta} = pR, \; N_{xx} = \dfrac{pR}{2}\right)$ and the principal strains $\left(\epsilon_{xx}^{o}\right)_{p}$ and $\left(\epsilon_{\theta\theta}^{o}\right)_{p}$ are measured. The tests provide four equations for determining the three stiffnesses. Three of the equations can be combined to yield

$$
\left.
\begin{aligned}
A_{22} &= \frac{pR}{\left(\epsilon_{\theta\theta}^{o}\right)_{p}} \Bigg/ \left[1 - \frac{\left(\epsilon_{\theta\theta}^{o}\right)_{T} \left(\epsilon_{xx}^{o}\right)_{p}}{\left(\epsilon_{xx}^{o}\right)_{T} \left(\epsilon_{\theta\theta}^{o}\right)_{p}} \right] \\[2em]
A_{11} &= \frac{\text{LOAD}}{\pi D \left(\epsilon_{xx}^{o}\right)_{T}} + A_{22} \left[\frac{\left(\epsilon_{\theta\theta}^{o}\right)_{T}}{\left(\epsilon_{xx}^{o}\right)_{T}} \right]^{2} \\[2em]
A_{12} &= - A_{22} \frac{\left(\epsilon_{\theta\theta}^{o}\right)_{T}}{\left(\epsilon_{xx}^{o}\right)_{T}}.
\end{aligned}
\right\}
\qquad \text{[C-10]}
$$

The fourth equation from the tests provides a check on A_{12}:

$$
A_{12} = \frac{pR}{2\left(\epsilon_{\theta\theta}^{o}\right)_{p}} - A_{11} \frac{\left(\epsilon_{xx}^{o}\right)_{p}}{\left(\epsilon_{\theta\theta}^{o}\right)_{p}}.
\qquad \text{[C-11]}
$$

The same procedure is applied to the torsion test. With no axial loads or internal pressure, Eq [C-9] yields

$$\epsilon_{xx}^{o} = - \frac{\left[2 \frac{B_{16}}{R} \left(A_{22} + \frac{D_{22}}{R^2} \right) - \frac{B_{26}}{R} A_{12} \right]}{\left[A_{11} \left(A_{22} + \frac{D_{22}}{R^2} \right) - A_{12}^2 \right]} \epsilon_{x\theta}^{o}$$

and then

$$N_{x\theta} = \left(A_{66} + \frac{D_{66}}{R^2} \right) \left\{ 1 - \frac{\left[2 \left(\frac{B_{16}}{R} \right)^2 \left(A_{22} + \frac{D_{22}}{R^2} \right) - \frac{B_{26}}{R} \frac{B_{16}}{R} A_{12} \right]}{\left(A_{66} + \frac{D_{66}}{R^2} \right) \left[A_{11} \left(A_{22} + \frac{D_{22}}{R^2} \right) - A_{12}^2 \right]} \right\} \epsilon_{x\theta}^{o}.$$

Again, for $(h/R)^2 \ll 1$, the bracket term is effectively unity and the constitutive equation used for determining A_{66} for the orthotropic cylinders is equally valid for the anisotropic cylinders, that is,

$$N_{x\theta} = A_{66} \epsilon_{x\theta}^{o} = 2 A_{66} \epsilon_{45°}$$

with $D_{66}/R^2 \ll A_{66}$. Therefore,

$$A_{66} = Torque \Big/ \left(4\pi R^2 \epsilon_{45°} \right) \qquad [C-12]$$

The engineering shear strain $\left(\epsilon_{x\theta}^{o} \right)$ is twice the tensile strain $\epsilon_{45°}$ measured at 45° with respect to the longitudinal direction. The proof is based on the usual Mohr's circle or second rank tensor transformation argument.

Once the [A] matrix is known, the composite moduli are obtained from the system of four independent algebraic equations represented by Eq [C-3], with Eq [C-7] used. The four equations can be symmetrized and the result is

$$
[M] \cdot
\begin{bmatrix}
C_{22}^c \\[2ex]
C_{11}^c \\[2ex]
C_{66}^c \\[2ex]
C_{12}^c
\end{bmatrix}
=
\begin{bmatrix}
A_{22} \\[2ex]
A_{11} \\[2ex]
4A_{66} \\[2ex]
2A_{12}
\end{bmatrix}
\tag{C-13}
$$

with the elements of the symmetric matrix [M] given by

$$M_{11} = 2h_c + h_p s^4$$

$$M_{12} = h_p c^4$$

$$M_{13} = 4h_p s^2 c^2$$

$$M_{14} = M_{13}/2$$

$$M_{22} = M_{11}$$

$$M_{23} = M_{13}$$

$$M_{24} = M_{14}$$

$$M_{33} = 4\left(2h_c + h_p \left(c^2 - s^2\right)^2\right)$$

$$M_{34} = -2M_{13}$$

$$M_{44} = 2\left(2h_c + h_p \left(c^4 + s^4\right)\right).$$

After Eq [C-13] is solved for the composite moduli by Crout reduction, the coupling and the bending stiffness matrices are obtained from Eq [C-4] and [C-5].

Two comments must now be made. First, since the magnitude of [B] does not affect the determination of stiffness and moduli, it seems reasonable to assume that the nonhomogeneity of [B] will not affect the analysis. Second, it is not theoretically necessary to obtain explicit expressions for the in-plane stiffness matrix before the composite moduli are computed. The moduli C_{22}^c, C_{11}^c, C_{12}^c, and C_{66}^c may be obtained directly from Eq [C-9] with the appropriate loading conditions specified and with Eq [C-1], [C-3], [C-4], and [C-7] used.

Finally, in order to provide a comparison with theoretical methods of computing moduli, computations have been made for

Major Poisson's ratio $= \nu_{12} = C_{12}^c \big/ C_{11}^c$

Minor Poisson's ratio $= \nu_{21} = C_{12}^c \big/ C_{22}^c$

Young's modulus
in direction of fibers $= E_{22}^c = C_{22}^c (1 - \nu_{12} \cdot \nu_{21})$

Young's modulus
perpendicular to fibers $= E_{11}^c = C_{11}^c (1 - \nu_{12} \cdot \nu_{21})$

with

Shear modulus $= C_{66}^c$.

[C-14]
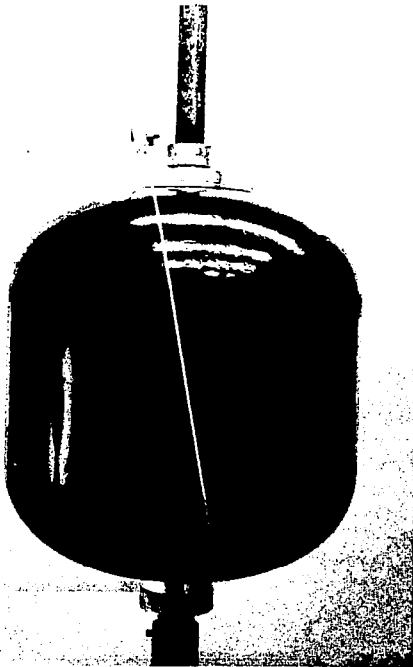
Fig. C-2 Front View of First
          Polar Encirclement of
          Roving Around Mandrel
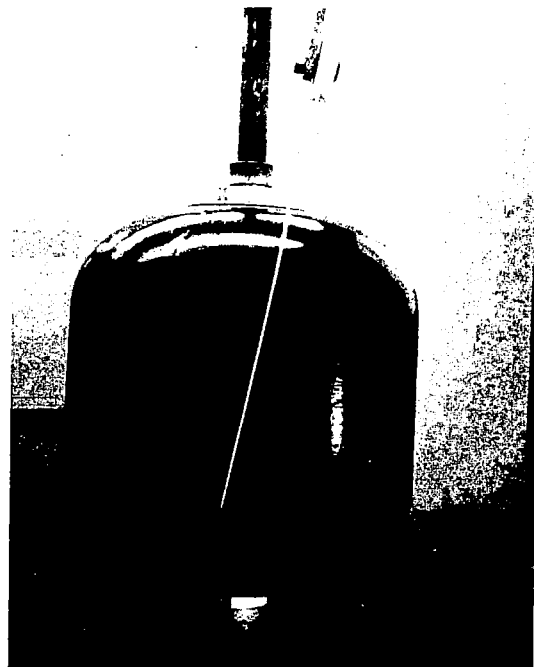

Fig. C-3 Rear View of First
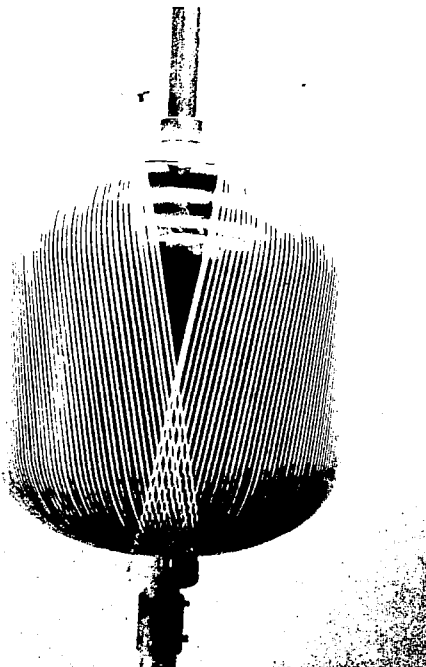   Polar Encirclement of
          Roving Around Mandrel

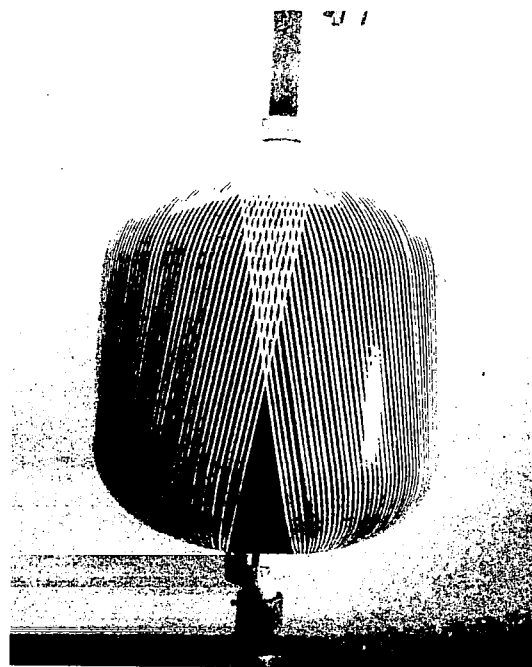Fig. C-4 Front View after Mandrel
          Has Rotated 180 deg

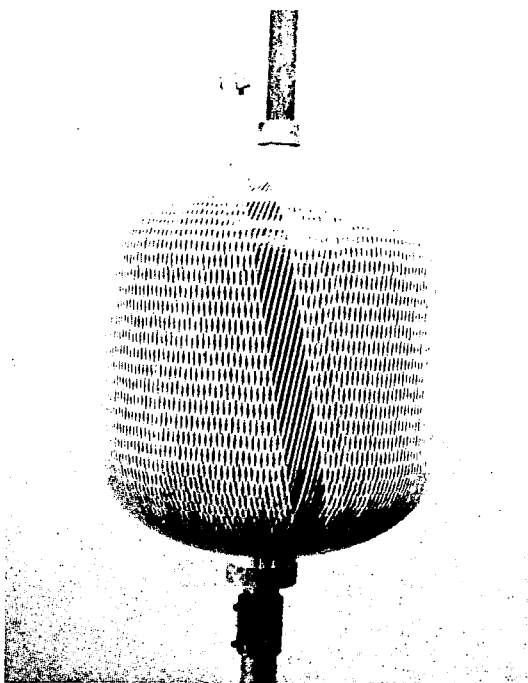Fig. C-5 Rear View after Mandrel
          Has Rotated 180 deg

57

Fig. C-6   Front View Just Before Mandrel has Completed a 360-deg Rotation
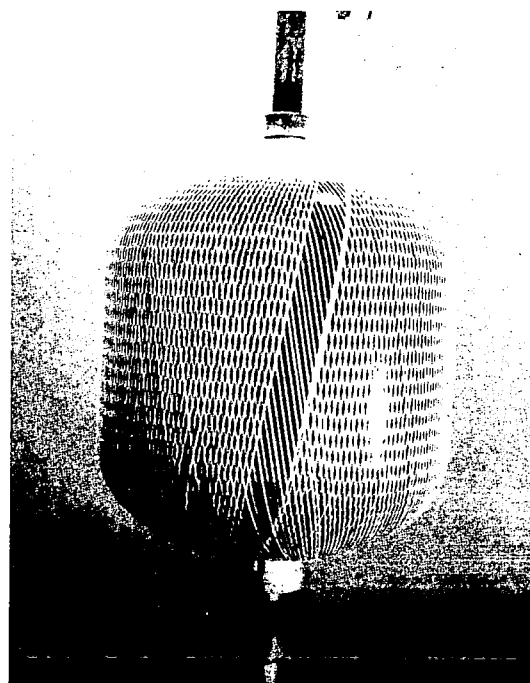

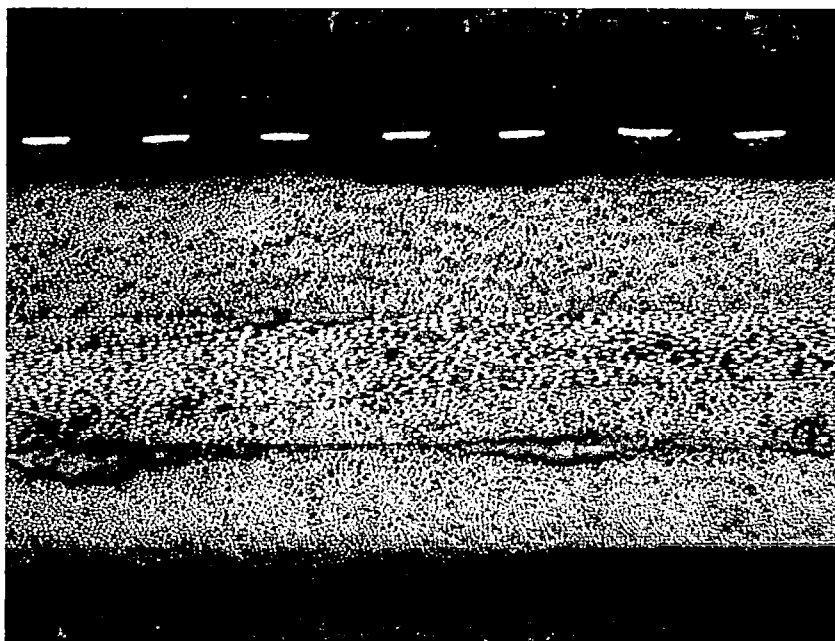Fig. C-7   Rear View Just Before Mandrel has Completed a 360-deg Rotation

Fig. C-8   Photomicrograph of Weave "Line" in Cylinder 1 (60X). Surface is 30 deg with Respect to the Axis of the Cylinder. Gage 10 is also shown.